Journal of Magnetic Resonance **139,** 314–333 (1999)
Article ID jmre.1999.1786, available online at http://www.idealibrary.com on IDEAL®

Separation of ^{2}H MAS NMR Spectra by Two-Dimensional Spectroscopy

J. H. Kristensen,[1] H. Bildsøe, H. J. Jakobsen, and N. C. Nielsen

Department of Chemistry, University of Aarhus, DK-8000 Aarhus C, Denmark

Received December 14, 1998; revised April 1, 1999

New methods for optimum separation of ^{2}H MAS NMR spectra are presented. The approach is based on hypercomplex spectroscopy that is useful for sign discrimination and phase separation. A new theoretical formalism is developed for the description of hypercomplex experiments. This exploits the properties of Lie algebras and hypercomplex numbers to obtain a solution to the Liouville–von Neumann equation. The solution is expressed in terms of coherence transfer functions that describe the allowed coherence transfer pathways in the system. The theoretical formalism is essential in order to understand all the features of hypercomplex experiments. The method is applied to the development of two-dimensional quadrupole-resolved ^{2}H MAS NMR spectroscopy. The important features of this technique are discussed and two different versions are presented with widely different characteristics. An improved version of two-dimensional double-quantum ^{2}H MAS NMR spectroscopy is developed. The conditions under which the double-quantum experiment is useful are discussed and its performance is compared with that observed for the quadrupole-resolved experiments. A general method is presented for evaluating the optimum pulse sequence parameters consistent with maximum sensitivity and resolution. This approach improves the performance of the experiments and is essential for any further development of the techniques. The effects of finite pulse width and hypercomplex data processing may lead to both intensity and phase distortions in the spectra. These effects are analyzed and general correction procedures are suggested. The techniques are applied to polycrystalline malonic-acid-$^2H_4$ for which the spinning sideband manifolds from the carboxyl and methylene deuterons are separated. The spinning sideband manifolds are simulated to determine the quadrupole parameters. The values are consistent with previous results, indicating that the techniques are both accurate and reliable.

Key Words: **separation of deuteron MAS NMR spectra; hypercomplex spectroscopy; quadrupole-resolved and double-quantum experiments; Lie algebra and coherence transfer; optimum pulse sequence parameters.**

INTRODUCTION

The characteristic lineshapes observed in deuteron (^{2}H) NMR spectroscopy are used extensively for the investigation of molecular structure and dynamics in a wide variety of solid materials (*1*). The most important property of deuteron spectra is that the lineshapes are dominated by the quadrupole interaction. This is characterized by the quadrupole coupling constant C_Q and the asymmetry parameter η_Q. For deuterons the quadrupole coupling constant is known to be relatively small ($C_Q \leq 250$ kHz) and because the quadrupole interaction is dominated by intramolecular contributions from the axially symmetric deuteron bond the asymmetry parameter is close to zero ($\eta_Q \leq 0.10$). These features result in relatively simple spectra and lineshapes that are sensitive to both molecular structure and motion.

The most important limitation of the method is that finite receiver recovery time may result in severe distortions of the spectra. This is understood from the fact that the quadrupole interaction results in a decay of the signal that is usually shorter than the time required for receiver recovery. It is therefore impossible to acquire an undistorted signal within the short decay period. This problem has been overcome by the quadrupole echo technique (*2, 3*) where a pulse sequence is used to form an echo at a time after the last pulse that is longer than the receiver recovery time. Because deuterons have a relatively narrow isotropic shielding range quadrupole echo spectra of polycrystalline systems with several structurally nonequivalent sites are not resolved unless the quadrupole parameters differ widely. This implies that the quadrupole echo experiment is most useful for selectively labeled samples. Another limitation is that the long delay periods in the quadrupole echo sequences may result in severe intensity loss (*4*).

The use of deuteron magic angle spinning (MAS) NMR spectroscopy has been suggested as a method for avoiding the problems with overlapping spectra (*5–9*). In this method mechanical rotation of the sample is used to impart a coherent averaging of the quadrupole interaction. The rotation frequency is usually less than the magnitude of the quadrupole interaction and the averaging results in a manifold of narrow spinning sidebands. This improves both the resolution and the sensitivity and the success of the method is documented by numerous examples. For polycrystalline samples with several structurally nonequivalent sites the spinning sideband manifolds overlap. Although this does not necessary affect the resolution it is inconvenient and may complicate the analysis of the spectra. For many important systems the spectra are non-

[1] Present address: Department of Physics, College of William and Mary, P.O. Box 8795, Williamsburg, VA 23187-8795.

1090-7807/99 $30.00

symmetric because of anisotropic shielding or paramagnetic shifts (*10–12*). In these cases the assignment of overlapping sidebands is difficult and can often only be done by recording the spectra with different rotation frequencies.

This suggests the use of two-dimensional techniques (*13*) to separate the spinning sideband manifolds. A recent example is two-dimensional one-pulse (TOP) spectroscopy (*14*). In this experiment the separation of the spectra is achieved by restricting the length of the evolution period to an integer multiple of the rotation period and recording the decay of one rotational echo in the detection period. The TOP spectra are represented by broad lineshapes, which imply a significantly reduced sensitivity. Because the TOP experiment includes no mixing period a nonsymmetric disposition of coherence transfer pathways is enforced in the evolution period. The spectra are therefore represented by a superposition of absorption–absorption, absorption–dispersion, dispersion–absorption, and dispersion–dispersion lineshapes (*15–17*). This feature is highly undesirable because the dispersion components reduce the resolution significantly.

In this paper several alternative methods are investigated for separating spinning sideband manifolds. The simplest approach is two-dimensional quadrupole-resolved one-pulse ^{2}H MAS NMR spectroscopy. In this experiment the spinning sideband manifolds are separated by restricting the length of the evolution period to an integer multiple of the rotation period and recording the train of rotational echoes in the detection period. The experiment includes no mixing period and the time domain signal may be obtained simply and efficiently by time shifting the train of rotational echoes. Whereas the resolution is similar to that achieved in the TOP experiment the sensitivity is improved by reducing the spectra to a manifold of spinning sidebands. To increase the resolution the two-dimensional quadrupole-resolved two-pulse ^{2}H MAS NMR experiment is proposed. This experiment is characterized by a symmetric disposition of coherence transfer pathways in the evolution period. The spectra may therefore be represented by pure absorption–absorption lineshapes which result in an improved resolving power.

It is noted that both two- and three-pulse ^{2}H MAS NMR experiments have been presented in the literature for separating paramagnetic and quadrupole interactions in solids (*18*). These experiments are complementary to the one- and two-pulse quadrupole-resolved experiments introduced in this paper. The previously proposed two-pulse experiment is not phase sensitive whereas the three-pulse sequence makes it possible to obtain pure absorption–absorption lineshapes. The most important disadvantage of these experiments is that the pulse sequences are highly susceptible to effects of finite pulse width although the three-pulse sequence compensates somewhat for the distortions. Moreover, for both pulse sequences it is difficult to realize the exact pulse rotation angles and this may introduce additional artifacts. The pulse sequences discussed in this paper do not have these disadvantages and are much easier to implement experimentally. It is obvious that the previously proposed experiments have several advantages for paramagnetic solids. However, our pulse sequences are designed to give optimum sensitivity and resolution and lead to spectra with a minimum of experimental artifacts. This implies that the approach presented here is superior for most solid materials.

The two-dimensional quadrupole-resolved ^{2}H MAS NMR experiments described above are not always sufficient to resolve overlapping powder spectra. This is the case when the residual linewidth of the individual spinning sidebands is comparable to the isotropic shielding range. This situation is common in the presence of molecular motion that contributes to the residual linewidth either directly or indirectly through a relaxation mechanism (*19*). Other contributions to the residual linewidth are second-order dipole and quadrupole interactions, instability of the rotation frequency, instability and inaccuracy of the angle setting, static field inhomogeneity, susceptibility inhomogeneity, and a distribution of shielding and quadrupole interactions. It is obvious that these contributions reduce the resolution and sensitivity and complicate the interpretation of the spectra. In this case the two-dimensional double-quantum ^{2}H MAS NMR experiment (*20–23*) presents opportunities for both resolution enhancement and spectral simplification. An important feature of the experiment is that the spectra are independent of the first-order quadrupole interaction and depend exclusively on the much smaller second-order quadrupole and first-order shielding interactions. The experiment is therefore less sensitive to the stability and accuracy of the angle setting. The resolving power of the double-quantum experiment is much better than that observed in the quadrupole-resolved experiments. However, because of line-broadening effects from the second-order quadrupole interaction, static field inhomogeneity, susceptibility inhomogeneity, and a distribution of shielding and quadrupole interactions the resolution enhancement is generally less than expected and depends on the actual lineshape. Another important property of the experiment is that the spectra provide information about structure and dynamics that is complementary to that derived from other techniques.

The inherent sensitivity of two-dimensional spectroscopy is relatively low, thereby impeding the general utility of the technique. In this paper an approach for optimizing the sensitivity and resolution is presented. This improves the performance of the experiments significantly and the results are obviously important for any further development of the techniques. The experiments are based on hypercomplex spectroscopy that has been used for more than a decade to obtain phase-sensitive spectra (*16, 17*). Although the hypercomplex data processing procedure is well known and used routinely on many spectrometers there has not been developed any complete theory to describe the form of hypercomplex spectra. It is a general assumption that the hypercomplex data processing procedure only leads to sign discrimination and phase separation. This is true in the case of ideal rf irradiation (strong and

short pulses) and for experiments with symmetric coherence transfer pathways in the evolution periods. However, for nonideal rf irradiation (weak and long pulses) that is often unavoidable in solid-state experiments the form of the hypercomplex spectra is not obvious. In order to simulate the spectra correctly it is necessary to take into account the effects of both nonideal rf irradiation and hypercomplex data processing. This paper presents a theoretical formalism based on density operator algebra for calculating hypercomplex spectra. The formalism is used to describe the phase and intensity characteristics of the two-dimensional quadrupole-resolved and double-quantum ^{2}H MAS NMR experiments. It is shown how the results may be combined with an optimization procedure to obtain the best sensitivity and resolution. The approach is demonstrated experimentally by acquiring a series of spectra of polycrystalline malonic-acid-$^2H_4$. These are analyzed to obtain the quadrupole parameters for each structurally nonequivalent deuteron.

THEORY

Hypercomplex Spectroscopy

To provide the theoretical framework for hypercomplex spectroscopy this section describes the elements of hypercomplex density operator algebra. This formalism forms the basis for the development of the experiments described in the next sections. The experimental scheme consists of a preparation period and $N - 1$ mixing periods that separate $N - 1$ evolution periods of lengths $\tau_1, \ldots, \tau_{N-1}$ and a detection period of length τ_N. To sample the evolution periods a series of experiments is performed with systematic incrementation of $\tau_1, \ldots, \tau_{N-1}$. For each value of $\tau_1, \ldots, \tau_{N-1}$ the detection period is sampled in quadrature to define the time domain signal $z(\tau_1, \ldots, \tau_N)$. To obtain a convenient representation of the spectrum the time domain signal is Fourier transformed to define the frequency domain signal $Z(\omega_1, \ldots, \omega_N)$. In order to achieve sign discrimination in the $\omega_1, \ldots, \omega_N$ dimensions it is useful to implement quadrature detection in both the evolution and the detection periods. This reduces the rf power and data storage requirements to a minimum. Furthermore, to improve resolution and to avoid cancellation effects it is desirable to implement phase-sensitive spectroscopy whereby the phase may be adjusted independently in the $\omega_1, \ldots, \omega_N$ dimensions to suppress the dispersion components.

While quadrature detection in the detection period is straightforward to arrange (*24*) its accomplishment in the evolution periods has only been achieved in phase-sensitive spectroscopy by two complementary procedures. In one approach (*25*) the preparation and mixing propagators are subjected to Time Proportional Phase Incrementation (TPPI). In this procedure the phases $\varphi_1, \ldots, \varphi_{N-1}$ of the preparation and mixing propagators are incremented independently and systematically in proportion to $\tau_1, \ldots, \tau_{N-1}$. This is expressed by

$$\varphi_k = \frac{3\pi}{2\Delta m_k}\frac{\tau_k}{\Delta\tau_k}, \qquad [1]$$

where $\Delta m_1, \ldots, \Delta m_{N-1}$ are the orders of coherence at the beginning of the respective evolution periods and $\Delta\tau_1, \ldots, \Delta\tau_{N-1}$ are the corresponding sampling periods. In another approach (*16, 17*) a series of complementary experiments is performed that differ by $3\pi/2\Delta m_1, \ldots, 3\pi/2\Delta m_{N-1}$ radians in the phase of the coherences at the beginning of the respective evolution periods. The phase shifts may be realized by incorporating into the phase cycle elements in which the phases of the preparation and mixing propagators are defined independently by

$$\varphi_k = \left\{0, \frac{3\pi}{2\Delta m_k}\right\}. \qquad [2]$$

This scheme represents a succession of 2^{N-1} independent experiments for each of which the time domain signal is kept separate and stored as a component of a hypercomplex time domain signal. Pure phase lineshapes are obtained by subjecting the time domain signal to a hypercomplex Fourier transformation. It is noted that the performance of the hypercomplex experiment is not degraded because each of the 2^{N-1} components is recorded with the number of transients reduced by a factor of 2^{N-1}.

For phase-sensitive spectroscopy both methods presuppose that two symmetrically disposed coherence transfer pathways are retained by phase cycling in each evolution period and that the coherence transfer functions have equal amplitude. The procedures therefore require that a total of 2^{N-1} different coherence transfer pathways be retained. Furthermore, the methods are only applicable for pure amplitude-modulated time domain signals. The procedures have equal performance and data storage requirements and the only differences are defined by the data handling procedures and the type of Fourier transformation applied with respect to $\tau_1, \ldots, \tau_{N-1}$. This section develops a theoretical framework for describing hypercomplex experiments that represents a generalization of previous approaches by including arbitrary coherence transfer processes and experiments of arbitrary dimension.

The approach is based on hypercomplex numbers (*26*) that are spanned by the hyperimaginary units $i_1, \ldots, i_N$ and all their distinct products. The hyperimaginary units satisfy the equations $i_m i_m = -1$, $i_m i_n = i_n i_m$, and $i_m(i_m i_n) = (i_m i_n) i_m = -i_n$. It is important to note that the square root function is not defined for hypercomplex numbers. This implies that $i_m i_m = -1$ only has the trivial solution i_m that cannot be expressed as the square root of -1. If this had been the case the product $i_m i_n$ would have been equal to -1 and the hypercomplex numbers would be undefined. In hypercomplex spectroscopy it is convenient to describe the state of a statistical ensemble by the hypercomplex density operator

$$\sigma(t) = \sigma(t, \varphi_0) + \sum_{1\le p\le N-1} \sum_{1\le k_1\le \cdots \le k_p\le N-1} i_{k_1}\cdots i_{k_p}\sigma(t, \varphi_{k_1\cdots k_p}), \quad [3]$$

where $\sigma(t, \varphi_{k_1\ldots k_p})$ are the density operators for the individual experiments (*27*). These are identified by the phase angles $\varphi_{k_1\ldots k_p}$ used for quadrature detection. It is noted that the hypercomplex density operator is an entity that is introduced mainly for computational convenience. Its existence is justified by the fact that it is necessary to know the outcome of each individual experiment in order to determine the intensity and phase relations in the spectra. The density operators $\sigma(t, \varphi_{k_1\ldots k_p})$ evolve independently according to the hypercomplex Liouville–von Neumann equation

$$\frac{\partial}{\partial t}|\sigma(t, \varphi_{k_1\cdots k_p})\rangle = -i_N \mathrm{Ad}(H(t, \varphi_{k_1\cdots k_p}))|\sigma(t, \varphi_{k_1\cdots k_p})\rangle, \quad [4]$$

where $H(t, \varphi_{k_1\ldots k_p})$ are the individual Hamiltonians (*27*). These may be understood as components of the hypercomplex Hamiltonian

$$H(t) = H(t, \varphi_0) + \sum_{1\le p\le N-1} \sum_{1\le k_1\le \cdots \le k_p\le N-1} i_{k_1}\cdots i_{k_p}H(t, \varphi_{k_1\cdots k_p}). \quad [5]$$

Again the existence of the hypercomplex Hamiltonian is justified mainly because it gives a precise description of the hypercomplex experiment. With an initial condition the solution is

$$|\sigma(t, \varphi_{k_1\cdots k_p})\rangle = \mathrm{Ad}(F(t_0, t, \varphi_{k_1\cdots k_p}))|\sigma(t_0, \varphi_{k_1\cdots k_p})\rangle, \quad [6]$$

where Ad is the adjoint representation (*28*) and the propagator

$$F(t_0, t, \varphi_{k_1\cdots k_p}) = T\exp\left(-i_N\int_{t_0}^{t} H(\tau, \varphi_{k_1\cdots k_p})d\tau\right). \quad [7]$$

In order to provide a complete description of the coherence transfer processes in the nuclear spin ensemble it is useful to exploit the properties of the corresponding Lie algebra (*28*). Because the group generators I_m are orthogonal and complete the density operator may be expressed as

$$\sigma(t, \varphi_{k_1\cdots k_p}) = \sum_m \sigma_m(t, \varphi_{k_1\cdots k_p})I_m, \quad [8]$$

where

$$\sigma_m(t, \varphi_{k_1\cdots k_p}) = \frac{\langle I_m|\sigma(t, \varphi_{k_1\cdots k_p})\rangle}{\langle I_m|I_m\rangle} \quad [9]$$

define the alignments and coherences of the nuclear spin ensemble. In this approach the time evolution of the system is described by

$$\sigma_n(t, \varphi_{k_1\cdots k_p}) = \sum_m f_{nm}(t_0, t, \varphi_{k_1\cdots k_p})\sigma_m(t_0, \varphi_{k_1\cdots k_p}), \quad [10]$$

where the coherence transfer functions

$$f_{mn}(t_0, t, \varphi_{k_1\cdots k_p}) = \frac{\langle I_m|\mathrm{Ad}(F(t_0, t, \varphi_{k_1\cdots k_p}))|I_n\rangle}{\langle I_m|I_m\rangle} \quad [11]$$

provide all the information about the time evolution of the system (*28*). This is represented by a series of coherence transfer processes. As an example the coherence transfer function $f_{nm}(t_0, t, \varphi_{k_1\ldots k_p})$ describes the transfer from a state $\sigma_m(t_0, \varphi_{k_1\ldots k_p})$ to $\sigma_n(t, \varphi_{k_1\ldots k_p})$ during the period from t_0 to t. This formalism is very convenient for describing the state of a nuclear spin ensemble and for keeping track of the various coherence transfer processes in the system.

The Lie algebra formalism is probably unfamiliar to most spectroscopists and one may ask whether it is essential for the analysis of the experiments. The first thing to note is that the usual density operator formalism is completely equivalent to a Lie algebra approach based on single transition step operators and polarization operators (*13*). This demonstrates that there is no fundamental difference in the two different approaches. Thus, all the results presented in this paper could in principle have been derived by standard density operator algebra. However, there are several important advantages of the Lie algebra approach. One important distinction is in the description of the states of the nuclear spin ensemble and the allowed coherence transfer pathways. The usual density operator algebra identifies the states by the coherence order and coherence transfer processes are described simply by the difference in coherence order. For many applications this simplification may be justified but for a complete description of the states and coherence transfer pathways the Lie algebra approach is necessary. An example is given by a deuteron spin system for which density operator algebra identifies only two single-quantum coherences of orders one and minus one, respectively. However, with the group generators defined by irreducible tensor operators (*28*) the Lie algebra approach identifies four different single-quantum coherences that are defined as dipoles and quadrupoles depending on the multipole character of the states. This methodology makes a distinction between coherences of the same order and clearly gives a much more detailed description of the state of the nuclear spin ensemble. Similarly, the density op-

erator approach identifies a coherence transfer process only by the difference in coherence order. This implies that any coherence transfer pathway is defined by a superposition of several nonequivalent coherence transfer processes. The Lie algebra approach on the other hand identifies all nonequivalent coherence transfer processes, thereby providing a much more detailed description of any experiment.

Another advantage of the Lie algebra approach is that one may exploit the symmetry properties of the system to reduce the number of coherence transfer pathways. Because the density operator approach is equivalent to the use of single transition step operators and polarization operators it is highly inefficient for the description of nonselective coherence transfer processes. However, in a Lie algebra approach based on irreducible tensor operators (*28*) the number of allowed coherence transfer processes is reduced significantly. This minimizes the computational effort and is reflected in much simpler expressions. As an example the number of coherence transfer functions involved in the calculations presented in this paper are reduced by a factor of 2 simply by implementing the irreducible tensor operators. Moreover, because all expressions are defined in terms of coherence transfer functions it is a simple matter to identify which coherence transfer pathways lead to the individual terms. This is important for optimizing the experiments because this is based on maximizing particular coherence transfer pathways.

The hypercomplex density operator may be expressed as a function of the lengths of the evolution and detection periods. The corresponding hypercomplex time domain signal is

$$z(\tau_1, \ldots, \tau_N) = \langle \sigma(\tau_1, \ldots, \tau_N) | I_+ \rangle, \qquad [12]$$

where $I_+ = I_x + i_N I_y$. The equation can be rewritten in the form

$$z(\tau_1, \ldots, \tau_N) = z(\tau_1, \ldots, \tau_N, \varphi_0) + \sum_{1 \le p \le N-1} \sum_{1 \le k_1 \le \cdots \le k_p \le N-1} i_{k_1} \cdots i_{k_p} \times z(\tau_1, \ldots, \tau_N, \varphi_{k_1 \cdots k_p}), \qquad [13]$$

where

$$z(\tau_1, \ldots, \tau_N, \varphi_{k_1 \cdots k_p}) = \langle \sigma(\tau_1, \ldots, \tau_N, \varphi_{k_1 \cdots k_p}) | I_+ \rangle \qquad [14]$$

are the time domain signals acquired in the individual experiments. The time domain signals can be rewritten in the form

$$z(\tau_1, \ldots, \tau_N, \varphi_{k_1 \cdots k_p}) = z_x(\tau_1, \ldots, \tau_N, \varphi_{k_1 \cdots k_p}) + i_N z_y(\tau_1, \ldots, \tau_N, \varphi_{k_1 \cdots k_p}), \qquad [15]$$

where

$$z_x(\tau_1, \ldots, \tau_N, \varphi_{k_1 \cdots k_p}) = \sigma_x(\tau_1, \ldots, \tau_N, \varphi_{k_1 \cdots k_p}),$$
$$z_y(\tau_1, \ldots, \tau_N, \varphi_{k_1 \cdots k_p}) = \sigma_y(\tau_1, \ldots, \tau_N, \varphi_{k_1 \cdots k_p}), \qquad [16]$$

represent two different phase quadrants. As a result a total of 2^N phase quadrants are defined which forms the basis for an independent phase adjustment in the $\omega_1, \ldots, \omega_N$ dimensions.

The hypercomplex frequency domain signal is defined by

$$Z(\omega_1, \ldots, \omega_N) = \int_{-\infty}^{\infty} \exp(-i_1 \omega_1 \tau_1) d\tau_1 \cdots \int_{-\infty}^{\infty} \times z(\tau_1, \ldots, \tau_N) \exp(-i_N \omega_N \tau_N) d\tau_N, \qquad [17]$$

which represents a hypercomplex Fourier transform of the time domain signal (*26*). In a hypercomplex experiment the time domain signal can be expressed in multicomplex form by

$$z(\tau_1, \ldots, \tau_N) = \prod_{k=1}^{N} f_k \exp([i_k \Omega_k - \lambda_k]\tau_k) \exp(i_k \varphi_k), \qquad [18]$$

where f_k are the amplitude factors, Ω_k the angular frequencies, λ_k the transverse relaxation rates, and φ_k the phase factors. It is noted that a multicomplex number is defined as a product of independent complex numbers (*26*). These are of particular interest in this context because they represent the only form for which pure absorption lineshapes can be obtained. Because any complex number has an exponential representation this definition is consistent with the above expression. The multicomplex frequency domain signal is

$$Z(\omega_1, \ldots, \omega_N) = \prod_{k=1}^{N} f_k [A_k(\omega_k - \Omega_k) + i_k D_k(\omega_k - \Omega_k)] \exp(i_k \varphi_k), \qquad [19]$$

where

$$A_k(\omega_k - \Omega_k) = \frac{\lambda_k}{\lambda_k^2 + [\omega_k - \Omega_k]^2},$$
$$D_k(\omega_k - \Omega_k) = \frac{\Omega_k - \omega_k}{\lambda_k^2 + [\omega_k - \Omega_k]^2}, \qquad [20]$$

are Lorentzian absorption and dispersion lineshapes, respectively. The phase factors may be eliminated by independent phase adjustment either before or after hypercomplex Fourier

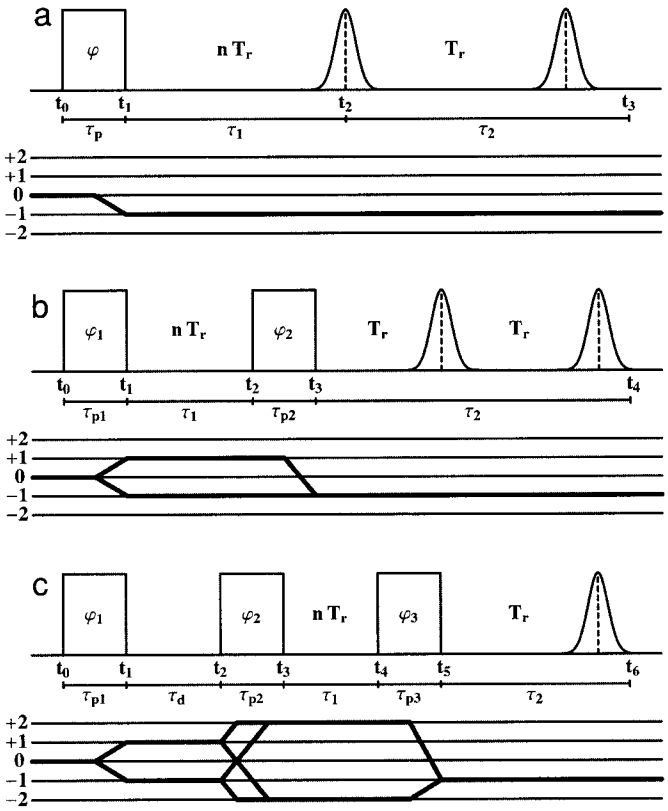

FIG. 1. Experimental schemes used for two-dimensional (a) quadrupole-resolved one-pulse, (b) quadrupole-resolved two-pulse, and (c) double-quantum ^{2}H MAS NMR spectroscopy.

transformation. This implies that the hypercomplex frequency domain signal may be represented in pure absorption mode.

Optimum Two-Dimensional Quadrupole-Resolved ^{2}H MAS NMR Spectroscopy

The simplest approach to separate ^{2}H MAS NMR spectra is the two-dimensional quadrupole-resolved one-pulse experiment. The pulse sequence that is illustrated in Fig. 1a involves nonselective rf irradiation and is characterized by a nonsymmetric disposition of coherence transfer pathways in the evolution period. The hypercomplex density operator is therefore expressed most conveniently in terms of irreducible SU(2) tensor operators for SU(3). However, in order to facilitate comparison with the other experiments described in this paper the hypercomplex density operator will be expressed consistently in terms of irreducible cartesian SU(2) tensor operators for SU(3). The form and properties of these operators are described elsewhere (*28*) and will not be discussed here.

The hypercomplex ^{2}H MAS NMR Hamiltonian can be approximated in the presence of rf irradiation by the truncated Magnus expansion

$$H(t,\,\varphi_0,\,\varphi_1) = \tilde{H}_{\mathrm{Q}}^{(1)}(t) + \tilde{H}_{\mathrm{rf}}^{(1)}(\varphi_0) + i_1[\tilde{H}_{\mathrm{Q}}^{(1)}(t) + \tilde{H}_{\mathrm{rf}}^{(1)}(\varphi_1)], \qquad [21]$$

which involves the first-order quadrupole and rf interactions (*29, 30*). In the absence of rf irradiation the hypercomplex Hamiltonian takes the form

$$H(t) = \tilde{H}_{\mathrm{Q}}^{(1)}(t) + \tilde{H}_{\mathrm{Q}}^{(2)}(t) + \tilde{H}_{\mathrm{CS}}^{(1)}(t) + i_1[\tilde{H}_{\mathrm{Q}}^{(1)}(t) + \tilde{H}_{\mathrm{Q}}^{(2)}(t) + \tilde{H}_{\mathrm{CS}}^{(1)}(t)], \qquad [22]$$

where the first- and second-order quadrupole and first-order shielding interactions are included. The individual interactions may be expressed in terms of irreducible cartesian SU(2) tensor operators for SU(3) to give

$$\begin{aligned}
\tilde{H}_{\mathrm{rf}}^{(1)}(\varphi) &= \omega_{\mathrm{rf}}[\cos(\varphi)I_x + \sin(\varphi)I_y],\\
\tilde{H}_{\mathrm{Q}}^{(1)}(t) &= \frac{1}{\sqrt{3}}\,\omega_{\mathrm{Q}}^{(1)}(t)I_{z^2},\\
\tilde{H}_{\mathrm{Q}}^{(2)}(t) &= \omega_{\mathrm{Q}}^{(2)}(t)I_z,\\
\tilde{H}_{\mathrm{S}}^{(1)}(t) &= \omega_{\mathrm{S}}^{(1)}(t)I_z,
\end{aligned} \qquad [23]$$

where $\omega_{\mathrm{Q}}^{(1)}(t)$ is the first-order quadrupole, $\omega_{\mathrm{Q}}^{(2)}(t)$ the second-order quadrupole, and $\omega_{\mathrm{S}}^{(1)}(t)$ the first-order shielding frequency (*28*). The angular transition frequencies are defined by

$$\begin{aligned}
\omega_{\mathrm{Q}}^{(1)}(t) &= \sqrt{3}A_{z^2}^{\mathrm{Q}}(t),\\
\omega_{\mathrm{Q}}^{(2)}(t) &= -\frac{1}{8\omega_0}\,[[A_{xz}^{\mathrm{Q}}(t)]^2 + [A_{yz}^{\mathrm{Q}}(t)]^2 + [A_{x^2-y^2}^{\mathrm{Q}}(t)]^2 + [A_{xy}^{\mathrm{Q}}(t)]^2],\\
\omega_{\mathrm{S}}^{(1)}(t) &= \frac{2\omega_0}{\sqrt{3}}\,A_{z^2}^{\mathrm{S}}(t) + \omega_{\mathrm{iso}},
\end{aligned} \qquad [24]$$

which are expressed in terms of the elements of the second-rank irreducible cartesian quadrupole and shielding tensors $\mathbf{A}_{\mathrm{Q}}^{(2)}$ and $\mathbf{A}_{\mathrm{S}}^{(2)}$. These can be obtained from

$$\begin{aligned}
\langle \mathbf{A}_{\mathrm{S}}^{(2)}(t)| &= \langle \mathbf{a}_{\mathrm{S}}^{(2)}(t)|\Gamma^{(2)}(\Omega_1)\Gamma^{(2)}(\Omega_2)\Gamma^{(2)}(\Omega_3(t)),\\
\langle \mathbf{A}_{\mathrm{Q}}^{(2)}(t)| &= \langle \mathbf{a}_{\mathrm{Q}}^{(2)}(t)|\Gamma^{(2)}(\Omega_2)\Gamma^{(2)}(\Omega_3(t)),
\end{aligned} \qquad [25]$$

where

$$\begin{aligned}
\mathbf{a}_{\mathrm{Q}}^{(2)} &= \frac{C_{\mathrm{Q}}}{4k[2k-1]}\,\{-\eta_{\mathrm{Q}},\,0,\,\sqrt{3},\,0,\,0\},\\
\mathbf{a}_{\mathrm{S}}^{(2)} &= \frac{1}{2}\,C_{\mathrm{S}}\{-\eta_{\mathrm{S}},\,0,\,\sqrt{3},\,0,\,0\}\,,
\end{aligned} \qquad [26]$$

are the principal second-rank irreducible cartesian quadrupole and shielding tensors (*28*). These are expressed in terms of the

quadrupole coupling constant C_Q, the shielding anisotropy C_S, the asymmetry parameter η_Q for the quadrupole interaction, and the asymmetry parameter η_S for the shielding interaction. The second-rank irreducible cartesian representation matrix $\Gamma^{(2)}(\Omega)$ defines the transformations (*28*). The relative orientation of the principal axes systems of the shielding and quadrupole tensors is given by the Euler angles $\Omega_1 = \{\alpha_1, \beta_1, \gamma_1\}$. The transformation from the principal axis system of the quadrupole tensor to the rotor-fixed axis system is specified by $\Omega_2 = \{\alpha_2, \beta_2, \gamma_2\}$. The relative orientation of the rotor- and laboratory-fixed axes systems is defined by $\Omega_3(t) = \{\omega_r t, \theta, 0\}$, where θ is the angle between the rotation axis and the magnetic field and ω_r is the angular rotation frequency.

The detailed evaluation of the hypercomplex time domain signal follows the general principles outlined in the previous section. The results reveal that

$$\begin{aligned} z(\tau_1, \tau_2) = {} & \sigma_z(t_0) \sum_{m=x,y} [f_{x,m}(t_2, t_3) + i_2 f_{y,m}(t_2, t_3)] \\ & \times [f_{m,y}(t_1, t_2) + i_1 f_{m,x}(t_1, t_2)] f_{y,z}(t_0, t_1, 0) \\ & + \sigma_z(t_0) \sum_{m=xz,yz} [f_{x,m}(t_2, t_3) + i_2 f_{y,m}(t_2, t_3)] \\ & \times [f_{m,xz}(t_1, t_2) - i_1 f_{m,yz}(t_1, t_2)] f_{xz,z}(t_0, t_1, 0), \end{aligned} \quad [27]$$

where the coherence transfer functions

$$\begin{aligned} & f_{y,y}(t_1, t_2) + i_1 f_{y,x}(t_1, t_2) \\ & \quad = f_{x,x}(t_1, t_2) - i_1 f_{x,y}(t_1, t_2) \\ & \quad = f_{xz,xz}(t_1, t_2) - i_1 f_{xz,yz}(t_1, t_2) \\ & \quad = f_{yz,yz}(t_1, t_2) + i_1 f_{yz,xz}(t_1, t_2) \\ & \quad = \cos(\theta_1(t_1, t_2)) \exp(i_1 \theta_2(t_1, t_2)), \\ & f_{y,y}(t_2, t_3) - i_2 f_{x,y}(t_2, t_3) \\ & \quad = f_{x,x}(t_2, t_3) + i_2 f_{y,x}(t_2, t_3) \\ & \quad = \cos(\theta_1(t_2, t_3)) \exp(i_2 \theta_2(t_2, t_3)), \\ & f_{y,xz}(t_2, t_3) - i_2 f_{x,xz}(t_2, t_3) \\ & \quad = -f_{x,yz}(t_2, t_3) - i_2 f_{y,yz}(t_2, t_3) \\ & \quad = \sin(\theta_1(t_2, t_3)) \exp(i_2 \theta_2(t_2, t_3)), \end{aligned} \quad [28]$$

are defined in terms of

$$\begin{aligned} \theta_1(t_0, t) &= \int_{t_0}^{t} \omega_Q^{(1)}(\tau) d\tau, \\ \theta_2(t_0, t) &= \int_{t_0}^{t} [\omega_Q^{(2)}(\tau) + \omega_S^{(1)}(\tau)] d\tau, \end{aligned} \quad [29]$$

which are the phase angles for the first-order quadrupole interaction and the second-order quadrupole and first-order shielding interaction, respectively.

The length of the evolution period must be an integer multiple of the rotation period $T_r = 2\pi/\omega_r$ for complete coherent averaging. With this restriction the coherence transfer functions in the evolution period simplify to

$$\begin{aligned} f_{y,y}(t_1, t_2) + i_1 f_{y,x}(t_1, t_2) &= f_{x,x}(t_1, t_2) - i_1 f_{x,y}(t_1, t_2) \\ &= f_{xz,xz}(t_1, t_2) - i_1 f_{xz,yz}(t_1, t_2) \\ &= f_{yz,yz}(t_1, t_2) + i_1 f_{yz,xz}(t_1, t_2) \\ &= \exp(i_1[\omega_{iso} + \omega_{QS}]\tau_1), \end{aligned} \quad [30]$$

where ω_{iso} is the angular isotropic shielding frequency and ω_{QS} is the angular centerband second-order quadrupole frequency. These terms represent the time-independent parts of the interactions and are not eliminated by the averaging process. In the detection period the coherence transfer functions may be expanded in the Fourier series

$$\begin{aligned} & f_{y,y}(t_2, t_3) - i_2 f_{x,y}(t_2, t_3) \\ & \quad = f_{x,x}(t_2, t_3) + i_2 f_{y,x}(t_2, t_3) \\ & \quad = \sum_{m=-\infty}^{\infty} a_m \exp(i_2[m\omega_r + \omega_{iso} + \omega_{QS}]\tau_2), \\ & f_{y,xz}(t_2, t_3) - i_2 f_{x,xz}(t_2, t_3) \\ & \quad = -f_{x,yz}(t_2, t_3) - i_2 f_{y,yz}(t_2, t_3) \\ & \quad = \sum_{m=-\infty}^{\infty} b_m \exp(i_2[m\omega_r + \omega_{iso} + \omega_{QS}]\tau_2), \end{aligned} \quad [31]$$

where the expansion coefficients a_m and b_m are subject to the restrictions

$$\begin{aligned} & a_{-m} = a_m, \qquad b_{-m} = -b_m, \\ & \sum_{m=-\infty}^{\infty} a_m = 1, \quad \sum_{m=-\infty}^{\infty} b_m = 0. \end{aligned} \quad [32]$$

From the above equations it can be deduced that the time domain signal takes the form

$$\begin{aligned} z(\tau_1, \tau_2) = {} & \sum_{m=-\infty}^{\infty} [i_1 z_{10}^{(m)} + i_2 z_{01}^{(m)}] \exp([i_1\Omega_1 - \lambda_1]\tau_1) \\ & \times \exp([i_2\Omega_2^{(m)} - \lambda_2]\tau_2), \end{aligned} \quad [33]$$

where

$$z_{10}^{(m)} = z_{01}^{(m)} = [a_m f_{y,z}(t_0, t_1, 0) + b_m f_{xz,z}(t_0, t_1, 0)]\sigma_z(t_0) \quad [34]$$

are the amplitude factors and

$$\Omega_1 = \omega_{iso} + \omega_{QS},$$
$$\Omega_2^{(m)} = m\omega_r + \omega_{iso} + \omega_{QS}, \quad [35]$$

define the angular transition frequencies. The time domain signal has been modified to include the transverse relaxation rates λ_1 and λ_2 in the evolution and detection periods, respectively. This approach does not reflect all the relaxation properties of the system but is generally sufficient to evaluate the lineshapes.

The frequency domain signal can be expressed in the form

$$Z(\omega_1, \omega_2) = \sum_{m=-\infty}^{\infty} [i_1 z_{10}^{(m)} + i_2 z_{01}^{(m)}] \times L_1(\omega_1 - \Omega_1) L_2(\omega_2 - \Omega_2^{(m)}), \quad [36]$$

where

$$L_1(\omega_1 - \Omega_1) = A_1(\omega_1 - \Omega_1) + i_1 D_1(\omega_1 - \Omega_1),$$
$$L_2(\omega_2 - \Omega_2^{(m)}) = A_1(\omega_2 - \Omega_2^{(m)}) + i_2 D_2(\omega_2 - \Omega_2^{(m)}), \quad [37]$$

are Lorentzian lineshapes. The equations reveal that sign discrimination has been achieved in both frequency dimensions and that a symmetric spinning sideband manifold with Lorentzian sidebands at $\{\omega_1, \omega_2\} = \{\Omega_1, \Omega_2^{(m)}\}$ defines the spectrum. For a system with several nonequivalent deuterons the spinning sideband manifolds are separated in the ω_1 dimension provided that the angular transition frequencies Ω_1 differ sufficiently. The spectrum is not multicomplex because of the nonsymmetric disposition of coherence transfer pathways in the evolution period. Thus, although sign discrimination has been achieved in both frequency domains it is impossible to obtain spectra that are represented by pure absorption–absorption lineshapes. This feature is undesirable because the dispersion components reduce the resolution.

Because the proportions of absorption and dispersion components are identical it is impossible to improve the resolution. However, the sensitivity may be increased by carefully adjusting the preparation pulse length to maximize the magnitude of the amplitude factors. This leads to optimum two-dimensional quadrupole-resolved one-pulse ^{2}H MAS NMR spectroscopy. Because of the inherently low sensitivity of two-dimensional spectroscopy this is an important element in the development of the technique. The optimum preparation pulse length is obtained by maximizing the function

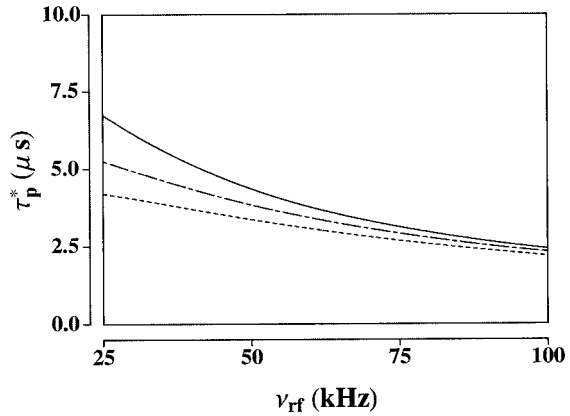

FIG. 2. The optimum preparation pulse length τ_p^* as a function of the rf field strength ν_{rf} for the quadrupole-resolved one-pulse ^{2}H MAS NMR experiment. The calculations employed the quadrupole coupling constants $C_Q = 100$ kHz (solid), $C_Q = 150$ kHz (dot-dashed), and $C_Q = 200$ kHz (dotted), asymmetry parameter $\eta_Q = 0.10$, and rotation frequency $\nu_r = 5.0$ kHz.

$$y(\tau_p) = |\sum_{m=-\infty}^{\infty} z_{10}^{(m)}|. \quad [38]$$

For a polycrystalline sample the amplitude factors differ among the crystallites and the object is to maximize the powder-integrated amplitude factors. The global maximum point τ_p^* is defined as the optimum preparation pulse length. This is shown in Fig. 2 as function of the rf field strength for different quadrupole coupling constants. In order to describe the results it is convenient to introduce the quantity $\Delta_p = \tau_p^0 - \tau_p^*$ that measures the difference between the optimum preparation pulse length obtained for nonideal (τ_p^*) and ideal ($\tau_p^0 = \pi/2\omega_{rf}$) rf irradiation. It is seen that Δ_p is a decreasing function of the rf field strength that converges asymptotically to zero and an increasing function of the quadrupole coupling constant. This is readily understood from the facts that the rf interaction is an increasing function of the rf field strength and that the quadrupole interaction is an increasing function of the quadrupole coupling constant.

The experiment makes it possible to obtain a separate ω_2 projection for each spinning sideband manifold. The projections are given by

$$Z(\tau_1 = 0, \omega_2) = \sum_{m=-\infty}^{\infty} [i_1 z_{10}^{(m)} + i_2 z_{01}^{(m)}] L_2(\omega_2 - \Omega_2^{(m)}), \quad [39]$$

which represents a symmetric spinning sideband manifold. It is seen that the spinning sidebands may be adjusted to have pure

absorption lineshapes. This is because the dispersion components cancel out in the projection. The amplitude factors depend on the coherence transfer functions for the first-order quadrupole and rf interactions. It is impossible to obtain exact expressions for these functions. However, the most important properties are defined by the first-order coherence transfer functions that give an accurate description of the time evolution of the system for short time intervals (*28*). The projections can be rewritten in terms of these to obtain

$$z(\tau_1 = 0,\ \tau_2) = -[i_1 + i_2]\sigma_z(t_0)\, D(t_0,\ t_1)\cos(\tfrac{1}{2}\theta_1(t_0,\ t_1) + \theta_1(t_2,\ t_3))\exp(i_2\theta_2(t_2,\ t_3)), \qquad [40]$$

where the intensity distortion function

$$D(t_0,\ t) = \frac{2\theta_p(t_0,\ t)}{\sqrt{\theta_1^2(t_0,\ t) + 4\theta_p^2(t_0,\ t)}} \times \sin\left(\frac{1}{2}\sqrt{\theta_1^2(t_0,\ t) + 4\theta_p^2(t_0,\ t)}\right) \qquad [41]$$

depends on both $\theta_1(t_0,\ t)$ and the pulse angle $\theta_p(t_0,\ t) = \omega_{rf}[t - t_0]$. For ideal rf irradiation the expression reduces to

$$z(\tau_1 = 0,\ \tau_2) = -[i_1 + i_2]\sigma_z(t_0)\sin(\theta_p(t_0,\ t_1)) \times \cos(\theta_1(t_2,\ t_3))\exp(i_2\theta_2(t_2,\ t_3)), \qquad [42]$$

which reveals that the projections obtained with nonideal rf irradiation are subject to both intensity and phase distortions. The effects of the intensity and phase distortions are demonstrated in Fig. 3, which includes projections calculated with both ideal and nonideal rf irradiation. The preparation pulse length has been adjusted to optimize the sensitivity of the experiment. For normally accessible rf field strengths the optimization enforces a considerable preparation pulse length which justifies a thorough investigation of the distortion effects. It is seen that the intensity distribution in the manifold of spinning sidebands is distorted in the spectra obtained with nonideal rf irradiation. The effect is to suppress the intensity of the high-order spinning sidebands whereas the low-order spinning sidebands are relatively unaffected. This is approximately described by the relative intensity distortion function

$$d(t_0,\ t,\ \omega) = \frac{\sin(\theta_p(t_0,\ t)\sqrt{1 + \omega^2/4\omega_{rf}^2})}{\sin(\theta_p(t_0,\ t))\sqrt{1 + \omega^2/4\omega_{rf}^2}}, \qquad [43]$$

which is analogous to that obtained for nonrotating samples (*3*). The results show a close agreement between the exact and approximate intensity ratios. This is unexpected because the equations predict that the intensity distortion for a single crystallite is distributed equally among all the spinning sidebands.

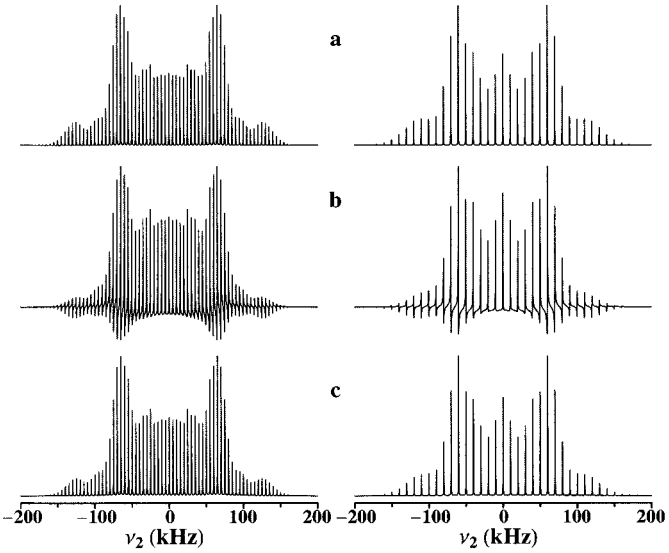

FIG. 3. Theoretical ω_2 projections for the quadrupole-resolved one-pulse ^{2}H MAS NMR experiment. The calculations used the quadrupole coupling constant C_Q = 200 kHz, asymmetry parameter η_Q = 0.10, and rotation frequencies ν_r = 5.0 kHz (left column) and ν_r = 10.0 kHz (right column). The figure represents spectra obtained under (a) ideal excitation conditions with the rf field strength ν_{rf} = 1000 kHz and optimum pulse length τ_p^* = 1.25 μs and (b) nonideal conditions with ν_{rf} = 25 kHz and τ_p^* = 4.25 μs. The phase distortion effects are demonstrated in (b) while (c) illustrates the result of a first-order phase correction.

The results can therefore only be explained by interference between subspectra from different crystallites (*31*). However, the relationship is important because the intensity distortions can be simulated very accurately by simple correction factors.

It is generally impossible to correct for the phase distortion introduced by nonideal rf irradiation. However, for small preparation pulse lengths time shifting can effectively eliminate the phase distortion. The form of the time domain signal shows that the condition for eliminating the phase distortion is

$$\tfrac{1}{2}\theta_1(t_0,\ t_1) + \theta_1(t_2,\ t_3 - \tau_s) = \theta_1(t_2,\ t_3), \qquad [44]$$

where τ_s is the time shift. The solution is approximated by $\tau_s = \frac{1}{2}\tau_p$ which is identical to that obtained for nonrotating samples (*3*). Multiplying the frequency domain spectrum by a first-order phase factor performs the phase correction most conveniently. The procedure shown in Fig. 3 also illustrates the effects of the phase distortion. It is noted that the first-order phase correction is remarkably good even for spectra acquired with large rotation frequencies.

The dispersion lineshapes inherent in the two-dimensional quadrupole-resolved one-pulse experiment are undesirable because of the reduced resolution and the possibility of cancellation effects. This suggests the introduction of a mixing period to redefine the coherence transfer pathways. The result is the

two-dimensional quadrupole-resolved two-pulse ^{2}H MAS NMR experiment. The experimental scheme illustrated in Fig. 1b reveals that the mixing period results in a symmetric disposition of coherence transfer pathways in the evolution period. The experiment therefore allows for pure absorption–absorption lineshapes. However, the actual lineshapes depend on the combined effects of nonideal rf irradiation and hypercomplex data processing. This may be made more explicit by considering the hypercomplex time domain signal that is similar to that obtained for the one-pulse experiment. The only difference is the amplitude factors that are given by

$$\begin{aligned} z_{10}^{(m)} = &[[\, f_{x,x}(t_2,\, t_3,\, 0)a_m - f_{yz,x}(t_2,\, t_3,\, 0)b_m]\, f_{y,z}(t_0,\, t_1,\, 0) \\ &+ [\, f_{yz,yz}(t_2,\, t_3,\, 0)b_m \\ &- f_{x,yz}(t_2,\, t_3,\, 0)a_m] \\ &\times f_{xz,z}(t_0,\, t_1,\, 0)]\sigma_z(t_0), \\ z_{01}^{(m)} = &[[\, f_{y,y}(t_2,\, t_3,\, 0)a_m + f_{xz,y}(t_2,\, t_3,\, 0)b_m]\, f_{y,z}(t_0,\, t_1,\, 0) \\ &+ [\, f_{xz,xz}(t_2,\, t_3,\, 0)b_m \\ &+ f_{y,xz}(t_2,\, t_3,\, 0)a_m] \\ &\times f_{xz,z}(t_0,\, t_1,\, 0)]\sigma_z(t_0). \end{aligned} \qquad [45]$$

The appearance of the spectra is therefore expected to be similar for the one- and two-pulse experiments. It is noted that the time domain signal is not multicomplex. The spinning sidebands are therefore represented by a superposition of absorption–absorption, absorption–dispersion, dispersion–absorption, and dispersion–dispersion lineshapes. However, an important difference exists in the phase characteristics of the one- and two-pulse experiments. In the two-pulse experiment two symmetrically disposed coherence transfer pathways are allowed in the evolution period and the phase distortion is the result of nonideal rf irradiation. This implies that the dispersion components vanish in the limit of ideal rf irradiation. For the one-pulse experiment the phase distortion is an inherent feature that derives from the nonsymmetric disposition of coherence transfer pathways. For the two-pulse experiment the form of the amplitude factors shows that the proportion of absorption components is significantly larger than the proportion of dispersion components. The result is that the two-pulse experiment has a superior resolving power.

The proportions of absorption and dispersion components depend on the relative magnitude of the amplitude factors and are subject to variation by the pulse sequence parameters. The proportion of dispersion components may be minimized under the constraint of maximum sensitivity by adjusting the pulse sequence parameters to maximize the magnitude of only one of the amplitude factors. This leads to optimum two-dimensional quadrupole-resolved two-pulse ^{2}H MAS NMR spectroscopy. The optimum pulse sequence parameters are obtained for a single crystallite by maximizing the function

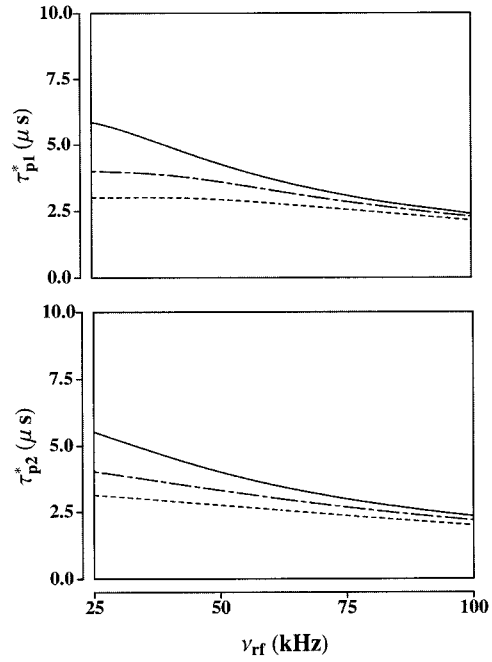

FIG. 4. The optimum preparation and mixing pulse lengths τ^*_{p1} and τ^*_{p2} as functions of the rf field strength ν_{rf} for the quadrupole-resolved two-pulse ^{2}H MAS NMR experiment. The calculations used the quadrupole coupling constants C_Q = 100 kHz (solid), C_Q = 150 kHz (dot-dashed), and C_Q = 200 kHz (dotted), asymmetry parameter η_Q = 0.10, and rotation frequency ν_r = 5.0 kHz.

$$y(\tau_{p1},\, \tau_{p2}) = \Big|\sum_{m=-\infty}^{\infty} z_{10}^{(m)}\Big| - \Big|\sum_{m=-\infty}^{\infty} z_{01}^{(m)}\Big|. \qquad [46]$$

For a polycrystalline sample the amplitude factors must be replaced by powder-integrated amplitude factors. The global maximum point defines the optimum preparation and mixing pulse lengths τ^*_{p1} and τ^*_{p2}. These are shown in Fig. 4 as functions of the rf field strength for different quadrupole coupling constants. In order to understand the results it is useful to introduce the quantities $\Delta_{p1} = \tau^0_{p1} - \tau^*_{p1}$ and $\Delta_{p2} = \tau^0_{p2} - \tau^*_{p2}$ that give the difference between the optimum preparation and mixing pulse lengths obtained with nonideal (τ^*_{p1} and τ^*_{p2}) and ideal ($\tau^0_{p1} = \tau^0_{p2} = \pi/2\omega_{rf}$) rf irradiation. It is seen that the functional dependence of Δ_{p1} and Δ_{p2} is similar to that observed in the one-pulse experiment for the same reasons originally noted. However, the values of the pulse sequence parameters differ and are generally significantly smaller. It is seen that the preparation and mixing pulse lengths are almost equal. The optimum pulse sequence is therefore approximately symmetric for all values of the rf field strength.

Optimum Two-Dimensional Double-Quantum ^{2}H MAS NMR Spectroscopy

The two-dimensional quadrupole-resolved two-pulse ^{2}H MAS NMR experiment improves the resolution significantly

by reducing the proportion of dispersion components. However, the inherent linewidth of the spinning sidebands may be a limiting factor for many systems. This is especially true for structurally or motionally disordered materials. In these cases a useful alternative is the two-dimensional double-quantum ^{2}H MAS NMR experiment (*20–23*). This technique has the potential of resolution enhancement and spectral simplification. However, as will be shown in this section the actual resolution enhancement depends on the lineshape and the technique is generally less useful for systems with large quadrupole coupling constants. The experimental scheme illustrated in Fig. 1c includes a representation of the allowed coherence transfer pathways. The hypercomplex time domain signal may be derived using the general formalism described above. An explicit calculation shows that

$$\begin{aligned} z(\tau_1, \tau_2) = \sigma_z(t_0) \sum_{m=y,xz} & [f_{x,m}(t_5, t_6) + i_2 f_{y,m}(t_5, t_6)] \\ & \times f_{m,xy}(t_4, t_5, 0)[f_{xy,x^2-y^2}(t_3, t_4) \\ & - i_1 f_{xy,xy}(t_3, t_4)][f_{x^2-y^2,z}(t_0, t_3, 0) \\ & + i_1 f_{xy,z}(t_0, t_3, 0)] + \sigma_z(t_0) \sum_{m=x,yz} \\ & \times [f_{x,m}(t_5, t_6) \\ & + i_2 f_{y,m}(t_5, t_6)] f_{m,x^2-y^2}(t_4, t_5, 0) \\ & \times [f_{x^2-y^2,x^2-y^2}(t_3, t_4) - i_1 f_{x^2-y^2,xy}(t_3, t_4)] \\ & \times [f_{x^2-y^2,z}(t_0, t_3, 0) + i_1 f_{xy,z}(t_0, t_3, 0)], \end{aligned} \quad [47]$$

which has been expressed in terms of the coherence transfer functions

$$\begin{aligned} f_{xy,z}(t_0, t_3, 0) = & [f_{xy,y}(t_2, t_3, 0) f_{y,y}(t_1, t_2) \\ & + f_{xy,xz}(t_2, t_3, 0) f_{xz,y}(t_1, t_2)] \\ & \times f_{y,z}(t_0, t_1, 0) \\ & + [f_{xy,xz}(t_2, t_3, 0) f_{xz,xz}(t_1, t_2) \\ & + f_{xy,y}(t_2, t_3, 0) f_{y,xz}(t_1, t_2)] \\ & \times f_{xz,z}(t_0, t_1, 0), \\ f_{x^2-y^2,z}(t_0, t_3, 0) = & [f_{x^2-y^2,x}(t_2, t_3, 0) f_{x,y}(t_1, t_2) \\ & + f_{x^2-y^2,yz}(t_2, t_3, 0) f_{yz,y}(t_1, t_2)] \\ & \times f_{y,z}(t_0, t_1, 0) \\ & + [f_{x^2-y^2,x}(t_2, t_3, 0) f_{x,xz}(t_1, t_2) \\ & + f_{x^2-y^2,yz}(t_2, t_3, 0) f_{yz,xz}(t_1, t_2)] \\ & \times f_{xz,z}(t_0, t_1, 0). \end{aligned} \quad [48]$$

It is noted that each term in these equations represents a coherence transfer pathway. The expressions therefore give a complete description of all allowed coherence transfer pathways in the experiment. The magnitude of $f_{xy,z}(t_0, t_3, 0)$ and $f_{x^2-y^2,z}(t_0, t_3, 0)$ which describe the transfer of dipole alignment into quadrupole double-quantum coherence during the preparation period is very small. This is reflected in the inherently low sensitivity of the double-quantum experiment.

For complete coherent averaging the length of the evolution period is restricted to an integer multiple of the rotation period. Although this is not strictly necessary for this experiment it may improve the performance by averaging any shielding anisotropy. With this restriction the coherence transfer functions in the evolution period become

$$\begin{aligned} & f_{x^2-y^2,x^2-y^2}(t_3, t_4) - i_1 f_{x^2-y^2,xy}(t_3, t_4) \\ & \quad = f_{xy,xy}(t_3, t_4) + i_1 f_{xy,x^2-y^2}(t_3, t_4) \\ & \quad = \exp(i_1 2[\omega_{iso} + \omega_{QS}]\tau_1), \end{aligned} \quad [49]$$

where it is noted that the angular isotropic shielding frequency and the angular centerband second-order quadrupole frequency are scaled by a factor of 2. In the detection period the coherence transfer functions are periodically time dependent and may be expanded in the Fourier series given by Eqs. [31] and [32]. With these relations the time domain signal becomes

$$\begin{aligned} z(\tau_1, \tau_2) = & \sum_{m=-\infty}^{\infty} [z_{00}^{(m)} + i_1 z_{10}^{(m)} + i_2 z_{01}^{(m)} + i_1 i_2 z_{11}^{(m)}] \\ & \times \exp([i_1\Omega_1 - \lambda_1]\tau_1)\exp([i_2\Omega_2^{(m)} - \lambda_2]\tau_2), \end{aligned} \quad [50]$$

which has been modified to include the transverse relaxation rates λ_1 and λ_2 in the evolution and detection periods, respectively. The amplitude factors are

$$\begin{aligned} z_{00}^{(m)} &= \sigma_z(t_0)[f_{x,x^2-y^2}(t_4, t_5, 0)a_m - f_{yz,x^2-y^2}(t_4, t_5, 0)b_m] \\ &\quad \times f_{x^2-y^2,z}(t_0, t_3, 0), \\ z_{10}^{(m)} &= \sigma_z(t_0)[f_{x,x^2-y^2}(t_4, t_5, 0)a_m - f_{yz,x^2-y^2}(t_4, t_5, 0)b_m] \\ &\quad \times f_{xy,z}(t_0, t_3, 0), \\ z_{01}^{(m)} &= \sigma_z(t_0)[f_{y,xy}(t_4, t_5, 0)a_m + f_{xz,xy}(t_4, t_5, 0)b_m] \\ &\quad \times f_{xy,z}(t_0, t_3, 0), \\ z_{11}^{(m)} &= -\sigma_z(t_0)[f_{y,xy}(t_4, t_5, 0)a_m + f_{xz,xy}(t_4, t_5, 0)b_m] \\ &\quad \times f_{x^2-y^2,z}(t_0, t_3, 0), \end{aligned} \quad [51]$$

and the angular transition frequencies

$$\begin{aligned} \Omega_1 &= 2[\omega_{iso} + \omega_{QS}], \\ \Omega_2^{(m)} &= m\omega_r + \omega_{iso} + \omega_{QS}. \end{aligned} \quad [52]$$

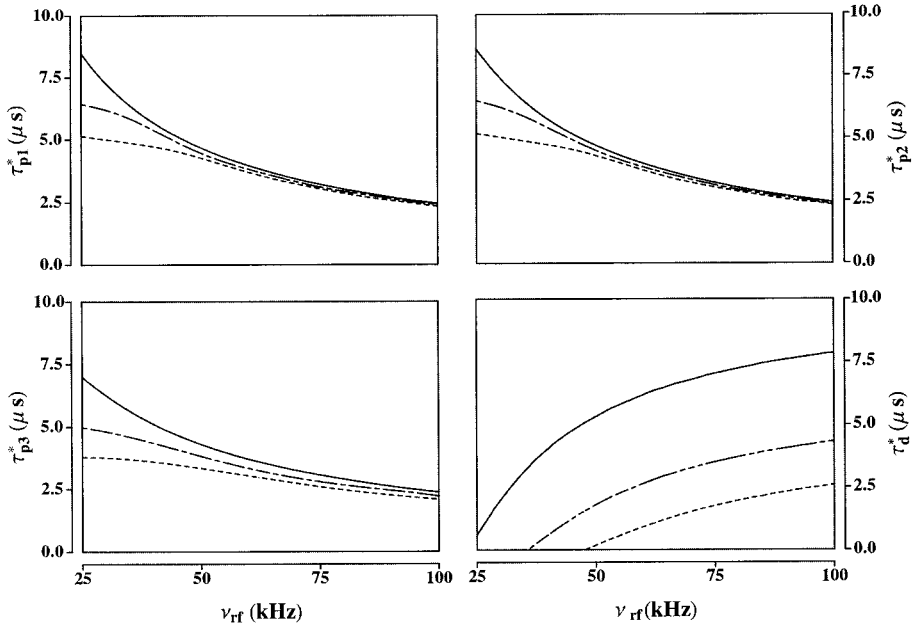

FIG. 5. The optimum preparation and mixing pulse lengths τ^*_{p1}, τ^*_{p2}, and τ^*_{p3} and optimum delay length τ^*_d as functions of the rf field strength ν_{rf} for the double-quantum ^{2}H MAS NMR experiment. The calculations employed the quadrupole coupling constants $C_Q = 100$ kHz (solid), $C_Q = 150$ kHz (dot-dashed), and $C_Q = 200$ kHz (dotted), asymmetry parameter $\eta_Q = 0.10$, and rotation frequency $\nu_r = 5.0$ kHz.

It is seen that the frequencies differ from those in the quadrupole-resolved experiments by a factor of 2 in the ω_1 dimension.

The hypercomplex frequency domain signal is given by

$$Z(\omega_1, \omega_2) = \sum_{m=-\infty}^{\infty} [z_{00}^{(m)} + i_1 z_{10}^{(m)} + i_2 z_{01}^{(m)} + i_1 i_2 z_{11}^{(m)}] \times L_1(\omega_1 - \Omega_1) L_2(\omega_2 - \Omega_2^{(m)}), \quad [53]$$

which shows that the spectrum is an antisymmetric spinning sideband manifold with Lorentzian sidebands at the angular frequencies $\{\omega_1, \omega_2\} = \{\Omega_1, \Omega_2^{(m)}\}$ and that sign discrimination has been achieved in both frequency dimensions. For a system with several nonequivalent deuterons the spectrum is a superposition of spinning sideband manifolds. Provided that the frequencies Ω_1 differ sufficiently the spinning sideband manifolds are separated in the ω_1 dimension. For a polycrystalline sample the angular dependence of the centerband second-order quadrupole frequency imposes a characteristic lineshape on the spinning sidebands that for systems with large quadrupole coupling constants may reduce the resolution. It is noted that the experiment does not lead to any resolution enhancement if the lineshape is dominated by the centerband second-order quadrupole frequency. On the other hand for small quadrupole coupling constants where the lineshape is not determined by the centerband second-order quadrupole frequency the experiment may improve the resolution by a factor of 2. The spectrum is not multicomplex and it is therefore impossible to obtain pure absorption–absorption lineshapes. Because the experiment is designed with a symmetric disposition of coherence transfer pathways in the evolution period this derives exclusively from nonideal rf irradiation. As a result the individual spinning sidebands are represented by a superposition of absorption–absorption, absorption–dispersion, dispersion–absorption, and dispersion–dispersion lineshapes. This is an undesirable feature because of the reduced resolution and the possibility of cancellation effects.

The proportions of absorption and dispersion components depend on the relative magnitude of the amplitude factors and are subject to variation by the pulse sequence parameters. This implies that the proportion of dispersion components can be minimized under the constraint of maximum sensitivity by adjusting the pulse sequence parameters to maximize one of the amplitude factors. This leads to optimum two-dimensional double-quantum ^{2}H MAS NMR spectroscopy. It is noted that this approach is an essential part of the experiment because of its inherently low sensitivity. For a single crystallite the optimum pulse sequence parameters are obtained by maximizing the function

$$y(\tau_{p1}, \tau_{p2}, \tau_{p3}, \tau_d) = \left| \sum_{m=-\infty}^{\infty} \mathrm{sgn}(m)\, z_{01}^{(m)} \right|, \quad [54]$$

where the sign function selects the antisymmetric components of the amplitude factors. In the case of a polycrystalline sample

the amplitude factors must be replaced by powder-integrated amplitude factors. The global maximum points τ^*_{p1}, τ^*_{p2}, and τ^*_{p3} are defined as the optimum preparation and mixing pulse lengths and τ^*_d is the optimum delay length. These are illustrated in Fig. 5 as functions of the rf field strength for various quadrupole coupling constants. It is convenient to describe the results in terms of $\Delta_{p1} = \tau^0_{p1} - \tau^*_{p1}$, $\Delta_{p2} = \tau^0_{p2} - \tau^*_{p2}$, and $\Delta_{p3} = \tau^0_{p3} - \tau^*_{p3}$, which measure the differences between the optimum preparation and mixing pulse lengths obtained with nonideal (τ^*_{p1}, τ^*_{p2}, and τ^*_{p3}) and ideal ($\tau^0_{p1} = \tau^0_{p2} = \tau^0_{p3} = \pi/2\omega_{rf}$) rf irradiation. The quantity $\Delta_d = \tau^0_d - \tau^*_d$ gives the difference between the optimum delay periods for nonideal (τ^*_d) and ideal (τ^0_d) rf irradiation. The results show that Δ_{p1}, Δ_{p2}, Δ_{p3}, and Δ_d have a similar functional dependence as described for the one- and two-pulse experiments although the values of the pulse sequence parameters differ significantly. It is seen that the preparation pulse lengths τ^*_{p1} and τ^*_{p2} are almost identical. This implies that the optimum pulse sequence has an approximately symmetric preparation period for all values of the rf field strength. The optimum delay length τ^*_d converges to zero for small rf field strengths. In these cases the optimum three-pulse sequence becomes a two-pulse sequence.

The experiment makes it possible to obtain separate ω_2 projections for the individual spinning sideband manifolds. The projections are given by

$$Z(\tau_1 = 0,\ \omega_2) = \sum_{m=-\infty}^{\infty} [\, z_{00}^{(m)} + i_1 z_{10}^{(m)} + i_2 z_{01}^{(m)} + i_1 i_2 z_{11}^{(m)}] \times L_2(\omega_2 - \Omega_2^{(m)}), \qquad [55]$$

which represents an antisymmetric spinning sideband manifold. It is seen that it is impossible to obtain projections with pure absorption lineshapes. However, the proportion of dispersion components is reduced considerably by implementing optimum pulse sequence parameters. In the limit of ideal rf irradiation the dispersion components vanish completely. The most important features of the spectra are determined by the first-order coherence transfer functions (*28*). The time domain signal may be rewritten in terms of these to obtain

$$\begin{aligned} z(\tau_1 = 0,\ \tau_2) = {} & -\sigma_z(t_0)\, D(t_0,\ t_1)\, D(t_2,\ t_3)\, D(t_4,\ t_5) \\ & \times \sin(\tfrac{1}{2}\theta_1(t_0,\ t_1) + \theta_1(t_1,\ t_2) \\ & \quad + \tfrac{1}{2}\theta_1(t_2,\ t_3))\sin(\tfrac{1}{2}\theta_1(t_4,\ t_5) + \theta_1(t_5,\ t_6)) \\ & \times \cos(\theta_2(t_1,\ t_2))\exp(i_2\theta_2(t_5,\ t_6)), \end{aligned} \qquad [56]$$

which includes an intensity distortion function (Eq. [41]) for each pulse. For ideal rf irradiation the projections become

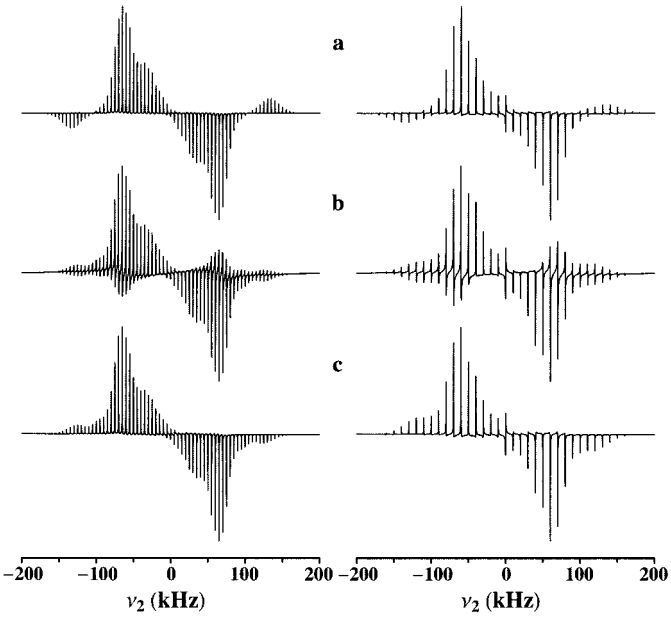

FIG. 6. Theoretical ω_2 projections for the double-quantum ^{2}H MAS NMR experiment. The calculations employed the quadrupole coupling constant $C_Q = 200$ kHz, asymmetry parameter $\eta_Q = 0.10$, and rotation frequencies $\nu_r = 5.0$ kHz (left column) and $\nu_r = 10.0$ kHz (right column). The figure represents spectra acquired under (a) ideal excitation conditions with the rf field strength $\nu_{rf} = 1000$ kHz and optimum pulse sequence parameters $\tau^*_{p1} = 1.25$ μs, $\tau^*_{p2} = 1.25$ μs, $\tau^*_{p3} = 1.25$ μs, and $\tau^*_d = 3.85$ μs and (b) nonideal conditions with $\nu_{rf} = 50$ kHz, $\tau^*_{p1} = 4.30$ μs, $\tau^*_{p2} = 4.30$ μs, $\tau^*_{p3} = 3.35$ μs, and $\tau^*_d = 0.15$ μs. The phase distortion effects are demonstrated in (b) while (c) illustrates the result of a first-order phase correction.

$$\begin{aligned} z(\tau_1 = 0,\ \tau_2) = {} & -\sigma_z(t_0)\sin(\theta_p(t_0,\ t_1))\sin(\theta_p(t_2,\ t_3)) \\ & \times \sin(\theta_p(t_4,\ t_5))\sin(\theta_1(t_1,\ t_2)) \\ & \times \sin(\theta_1(t_5,\ t_6))\cos(\theta_2(t_1,\ t_2))\exp(i_2\theta_2(t_5,\ t_6)), \end{aligned} \qquad [57]$$

which reveal that the spectra obtained with nonideal rf irradiation are subject to both intensity and phase distortions. These effects are shown in Fig. 6, which includes projections calculated for both nonideal and ideal rf irradiation. The optimization of the experiment enforces considerable preparation and mixing pulse lengths, justifying a thorough investigation of the intensity and phase distortions. The distortion suppresses the intensity of the high-order spinning sidebands while the low-order spinning sidebands show no significant effects. The relative distortion of the intensity distribution in the spinning sideband manifold can be represented approximately by

$$F(\omega) = d(t_0,\ t_1,\ \omega)d(t_2,\ t_3,\ \omega)d(t_4,\ t_5,\ \omega) \times \frac{\sin(\omega[\tfrac{1}{2}\tau_{p1} + \tfrac{1}{2}\tau_{p2} + \tau_d])}{\sin(\omega\tau_d)}, \qquad [58]$$

which includes the relative intensity distortion function (Eq. [43]) for each pulse. The computational results have shown that the approximate and exact intensity ratios are in close agreement. This relationship is important because the intensity distortion effects can be simulated very accurately and efficiently by simple correction factors.

The phase distortion induced by nonideal rf irradiation can be effectively eliminated by time shifting. The condition for eliminating the phase distortion is

$$\tfrac{1}{2}\theta_1(t_4, t_5) + \theta_1(t_5, t_6 - \tau_s) = \theta_1(t_5, t_6), \qquad [59]$$

where τ_s is the time shift. The approximate solution is $\tau_s = \frac{1}{2}\tau_{p3}$ which reveals that the phase distortion originates in the third pulse. The effects of the phase distortion are shown in Fig. 6, which also illustrates the phase correction procedure.

EXPERIMENTAL RESULTS

In order to demonstrate the essential features of the experiments a series of spectra of polycrystalline malonic-acid-$^2H_4$ has been recorded. This system is known to crystallize in a simple triclinic lattice structure (*32*). The unit cell holds only two molecules that are related by an inversion center. All molecules are therefore equivalent and the maximum number of lines is limited to 4. The composition of the molecule is almost ideal with deuterons at two different functional groups with widely different isotropic shielding frequencies. For the two-dimensional quadrupole-resolved one-pulse ^{2}H MAS NMR experiment the experimental spectra are shown in Fig. 7. Although the spinning sidebands are broadened by dispersion components the resolving power is sufficient to separate two different spinning sideband manifolds. These can be identified as arising from the carboxyl ($\nu_1 = 275$ Hz) and methylene ($\nu_1 = -275$ Hz) deuterons. The assignment was made on the basis of several independent observations. A point of particular importance is that the isotropic shielding frequency differs between the carboxyl and methylene deuterons. From empirical correlations it is known that carboxyl deuterons are shifted toward higher frequencies relative to methylene deuterons. Another important observation is that the spinning sideband manifolds are different for the carboxyl and methylene deuterons. These are determined by the quadrupole coupling constant and the asymmetry parameter which are generally larger for carboxyl deuterons than for methylene deuterons. The linewidths are seen to be different for the carboxyl and methylene deuterons. It is known (*33*) that the methylene deuterons are coupled by homonuclear dipole interactions that contribute to the linewidth. The sidebands are therefore broader for the methylene deuterons.

The experimental ω_2 projections are shown in Fig. 8 for both the carboxyl and methylene deuterons. The quadrupole parameters may be determined from these projections by simulating the spinning sideband manifolds. For the carboxyl deuterons it was found that $C_Q = 181$ kHz and $\eta_Q = 0.11$ while the methylene deuterons were simulated with $C_Q = 166$ kHz and $\eta_Q = 0.00$. The quadrupole parameters are identical to those previously obtained from polycrystalline samples (*7*) and single crystals (*34*). It is noted that the quadrupole coupling constant spans a much wider range than the isotropic shielding frequency. This suggests that the quadrupole coupling constant could offer a more sensitive means to differentiate between different types of deuterons than could the isotropic shielding frequency. The overall agreement between the experimental and theoretical spinning sideband manifolds is remarkable considering the inherent difficulty of two-dimensional spectroscopy. The small discrepancies that can be observed for some of the spinning sidebands are primarily the result of cancellation effects. From the experimentally determined quadrupole parameters the optimum preparation pulse length was calculated to be $\tau_p^* = 4.85$ μs. This result is consistent with $\tau_p^* = 5.25 \pm 0.50$ μs, which is obtained experimentally.

The importance of synchronizing the experiment accurately is demonstrated by the experimental spectra shown in Fig. 7. These reveal that the sidebands are displaced along the ω_1 dimension in nonsynchronized experiments. This reduces the resolution in the ω_1 dimension but has no effect on the resolution in the ω_2 dimension. The magnitude and direction of the displacements depend on the order of the sideband and the difference between the rotation frequency and the sampling frequency in the τ_1 dimension. The origin of the effect may be understood by considering the time domain signal

$$z(\tau_1, \tau_2) = \sum_{m=-\infty}^{\infty} [i_1 z_{10}^{(m)} + i_2 z_{01}^{(m)}] \times \exp(i_1 m\omega_r \tau_1)\exp(i_2 m\omega_r \tau_2), \qquad [60]$$

which for simplicity includes the effect of only the first-order quadrupole interaction. The frequency domain signal takes the form

$$Z(\omega_1, \omega_2) = \sum_{m=-\infty}^{\infty} [i_1 z_{10}^{(m)} + i_2 z_{01}^{(m)}] \times \delta(\omega_1 - m\omega_r)\delta(\omega_2 - m\omega_r), \qquad [61]$$

where $\delta(\omega)$ is the impulse function (*35*). The equation demonstrates that a symmetric spinning sideband manifold with sidebands at $\{\omega_1, \omega_2\} = \{m\omega_r, m\omega_r\}$ represents the spectrum. If the observations are made stroboscopically in the τ_1 dimension the time domain signal becomes

$$\hat{z}(\tau_1, \tau_2) = III(\tau_1) z(\tau_1, \tau_2), \qquad [62]$$

where $III(\tau)$ is the sampling function (*35*). The sampled frequency domain signal takes the form

$$\hat{Z}(\omega_1, \omega_2) = -\omega_{s1} \sum_{m=-\infty}^{\infty} \sum_{n=-\infty}^{\infty} [i_1 z_{10}^{(m)} + i_2 z_{01}^{(m)}] \times \delta(\omega_1 - m\omega_r - n\omega_{s1})\delta(\omega_2 - m\omega_r), \quad [63]$$

where ω_{s1} is the angular sampling frequency in the τ_1 dimension. The sampling frequency is given by $\omega_{s1} = \omega_r - \Delta\omega$, where $\Delta\omega$ is the degree to which the experiment is nonsynchronized. The frequency domain signal may therefore be rewritten in the form

$$\hat{Z}(\omega_1, \omega_2) = -\omega_{s1} \sum_{m=-\infty}^{\infty} \sum_{n=-\infty}^{\infty} [i_1 z_{10}^{(m)} + i_2 z_{01}^{(m)}] \times \delta(\omega_1 - [m+n]\omega_r + n\Delta\omega)\delta(\omega_2 - m\omega_r), \quad [64]$$

which includes all branches. The spectral width in the ω_1 dimension is limited by the sampling frequency in the τ_1 dimension. It is therefore possible to observe only the branch $m = -n$. This implies that

$$\hat{Z}(\omega_1, \omega_2) = -\omega_{s1} \sum_{m=-\infty}^{\infty} [i_1 z_{10}^{(m)} + i_2 z_{01}^{(m)}] \times \delta(\omega_1 - m\Delta\omega)\delta(\omega_2 - m\omega_r), \quad [65]$$

which demonstrates that the sidebands are at $\{\omega_1, \omega_2\} = \{m\Delta\omega, m\omega_r\}$ for spectra obtained in nonsynchronized experiments. The sidebands are displaced by $m\Delta\omega$ in the ω_1 dimension. The displacements are described by the angle $\theta = \arctan(\Delta\omega/\omega_r)$ which defines the orientation of the line passing through the centers of the sidebands. The equation shows that θ is a decreasing function of ω_r and an increasing function of $\Delta\omega$. The displacements are therefore less important for spectra acquired with high rotation frequencies. The direction of the displacements depends on whether the rotation frequency is higher or lower than the sampling frequency. In most experiments $\Delta\omega$ is close to zero and θ is therefore very small. However, even for small values of θ the displacements can be very large for the high-order spinning sidebands. For the spectra in Figs. 7b and 7c a simple measurement shows that the displacements are represented by $\theta = 5.9537 \times 10^{-3}$ and $\theta = -6.0572 \times 10^{-3}$, respectively. These values compare favorably with the theoretical values that are given by $\theta = 5.7755 \times 10^{-3}$ and $\theta = -5.7755 \times 10^{-3}$, respectively.

The performance of the two-dimensional quadrupole-resolved two-pulse ^{2}H MAS NMR experiment was evaluated from the experimental spectrum shown in Fig. 9a. Again the resolving power is sufficient to separate two spinning sideband manifolds from the carboxyl ($\nu_1 = 275$ Hz) and methylene ($\nu_1 = -275$ Hz) deuterons. By comparing the results it becomes apparent that the one-pulse experiment is superior in terms of sensitivity. This derives primarily from the efficient time shifting procedure and the large magnitude of the amplitude factors. However, the results reveal that the two-pulse experiment has a much better resolving power. Although not directly apparent from the contour plots the individual spinning sidebands are much narrower at the base in the two-pulse experiment. This is because the proportion of dispersion components is much smaller than the proportion of absorption components. For the one-pulse experiment the proportions of absorption and dispersion components are identical. It is important to note that the experimental ω_1 projections do not reflect the true resolving power of the experiments because the dispersion components are canceled out. Moreover, because the experiments are not perfectly synchronized the displacements of the spinning sidebands have a significant effect on the resolution in the ω_1 dimension. This shows that the one-pulse experiment is most advantageous for systems with low sensitivity and widely separated isotropic shielding frequencies while the two-pulse experiment is to be preferred for systems with high sensitivity and closely spaced isotropic shielding frequencies. From the experimentally determined quadrupole parameters the optimum pulse sequence parameters were found to be $\tau_{p1}^* = 3.50$ μs and $\tau_{p2}^* = 3.35$ μs. These results are consistent with the values $\tau_{p1}^* = 3.50 \pm 0.50$ μs and $\tau_{p2}^* = 3.50 \pm 0.50$ μs that are obtained experimentally.

In order to investigate the resolution enhancement in the two-dimensional double-quantum ^{2}H MAS NMR experiment a spectrum of polycrystalline malonic-acid-$^2H_4$ was recorded. The result shown in Fig. 9b demonstrates that the resolving power is sufficient to separate two spinning sideband manifolds. These can be identified as arising from the carboxyl ($\nu_1 = 550$ Hz) and methylene ($\nu_1 = -550$ Hz) deuterons. It is seen that the resolution in the ω_1 dimension has been increased by a factor of 2 compared with the resolution in the ω_2 dimension. This represents the maximum resolution enhancement in the experiment and is consistent with the fact that the spinning sidebands have no contribution from the second-order quadrupole interaction. For systems with larger quadrupole coupling constants the resolving power is expected to be much less. The experimental ω_2 projections shown in Fig. 10 have been simulated with the quadrupole coupling parameters $C_Q = 181$ kHz and $\eta_Q = 0.11$ for the carboxyl deuterons and with $C_Q = 166$ kHz and $\eta_Q = 0.00$ for the methylene deuterons. It is seen that the theoretical simulations represent all the essential features of the experimental ω_2 projections. The small discrepancies that can be observed for some of the spinning sidebands are the results of imperfect pathway selection and cancellation effects. Because the pathway selection is not perfect small amounts of dipole alignment and dipole and quad-

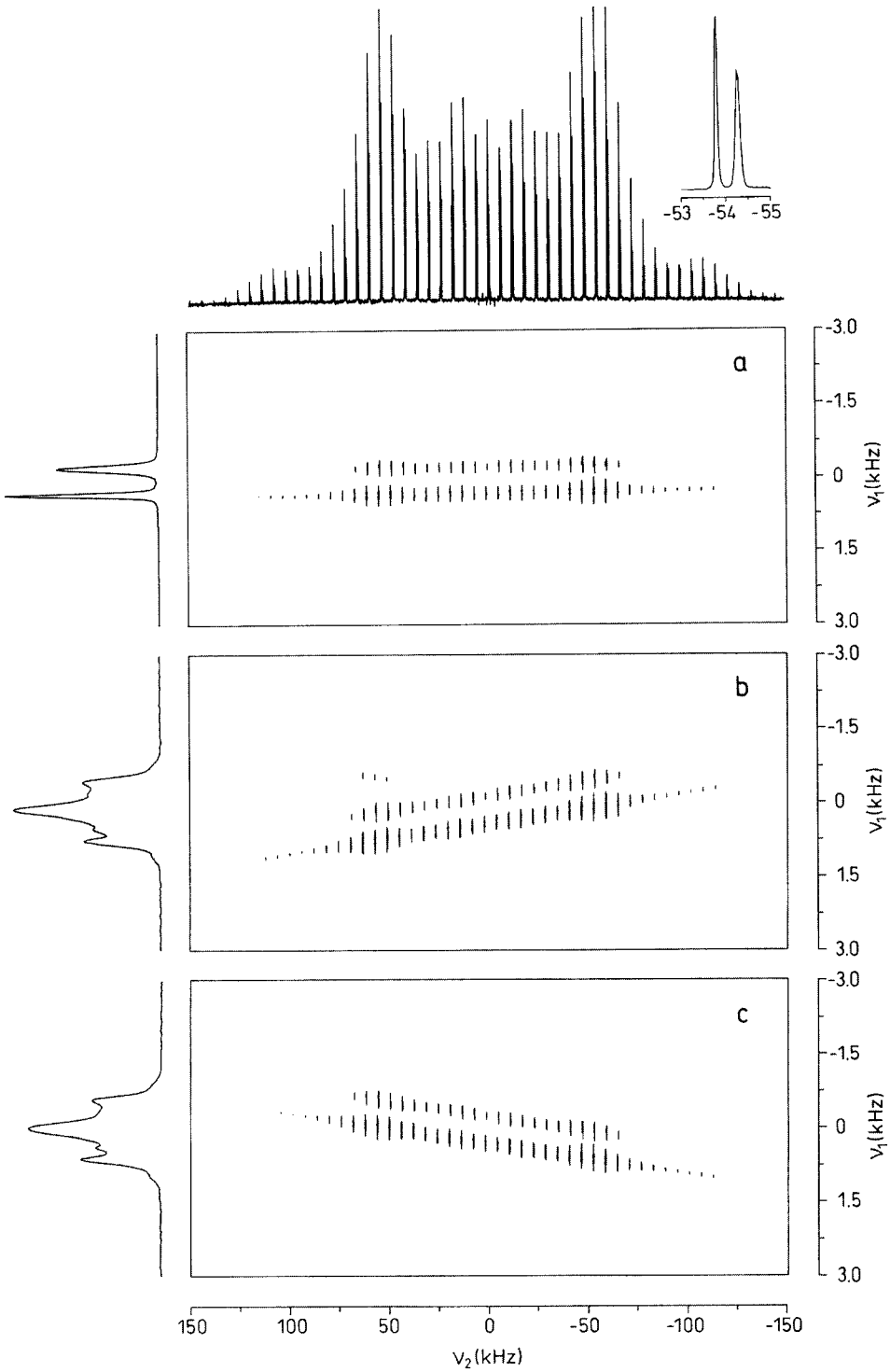

FIG. 7. Experimental quadrupole-resolved one-pulse ^{2}H MAS NMR spectra of polycrystalline [$^2H_4$]malonic acid. The spectra were recorded on a Varian VXR 400 S spectrometer with rotation frequencies (a) ν_r = 6060 Hz, (b) ν_r = 6095 Hz, and (c) ν_r = 6025 Hz. The rf field strength ν_{rf} = 22.5 ± 0.5 kHz and the optimum preparation pulse length τ_p^* = 5.25 ± 0.50 μs. For quadrature detection in the evolution period two complementary experiments (Eq. [2]) were performed which differ by $\frac{3\pi}{2}$ in the phase of the preparation pulse.

rupole single-quantum coherences are transferred to the evolution period. These contributions have a profound effect on the intensity distribution in the spinning sideband manifolds. From the experimentally determined quadrupole parameters the optimum pulse sequence parameters were calculated to be τ_{p1}^* = 5.75 μs, τ_{p2}^* = 5.95 μs, τ_{p3}^* = 4.45 μs, and τ_d^* = 0.00 μs.

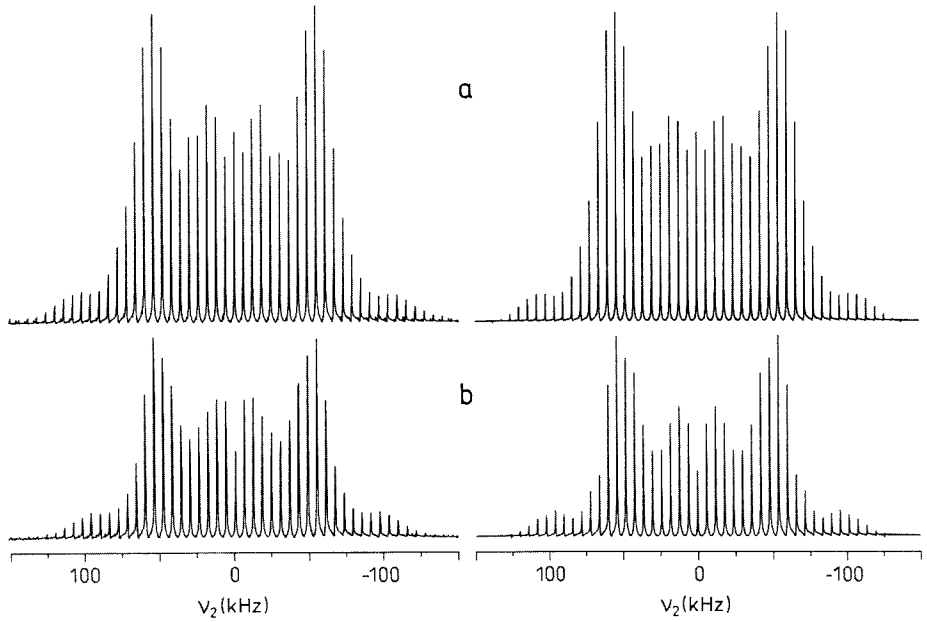

FIG. 8. Experimental (left column) and theoretical (right column) ω_2 projections for polycrystalline malonic-acid-$^2H_4$. The projections were obtained from the quadrupole-resolved one-pulse ^{2}H MAS NMR experiment. The calculations employed the quadrupole coupling constant C_Q = 181 kHz and asymmetry parameter η_Q = 0.11 for the carboxyl deuterons while C_Q = 166 kHz and η_Q = 0.00 for the methylene deuterons.

These results agree with the experimental values $\tau^*_{p1} = 5.25 \pm 0.50$ μs, $\tau^*_{p2} = 5.25 \pm 0.50$ μs, $\tau^*_{p3} = 5.00 \pm 0.50$ μs, and $\tau^*_d = 0.00 \pm 0.50$ μs. Because of the large number of variables it is generally very difficult to determine the optimum pulse sequence parameters experimentally. However, the quadrupole parameters may easily be determined from the intensity distribution in the spinning sideband manifolds. These parameters can be used to calculate the optimum pulse sequence parameters. The experiment is then repeated with the optimum pulse sequence parameters, resulting in a significant resolution and sensitivity improvement.

CONCLUSIONS

The techniques of optimum two-dimensional quadrupole-resolved and double-quantum ^{2}H MAS NMR spectroscopy that have been introduced in this paper are useful for separating overlapping spinning sideband manifolds from structurally nonequivalent deuterons. This paper presents a general methodology for evaluating the intensity and phase characteristics in these experiments. The formalism exploits the properties of hypercomplex numbers (*26*) and Lie algebras (*28*) to obtain a closed form solution to the Liouville–von Neumann equation. The solution is expressed in terms of coherence transfer functions that are useful for describing the states and allowed coherence transfer pathways in an arbitrary system. The results presented in this paper show that both the sensitivity and the resolution depend critically on the pulse sequence parameters. The exact relationship has been used to develop a general methodology for evaluating the optimum pulse sequence parameters consistent with maximum sensitivity and resolution. It has been demonstrated that the optimization introduces intensity and phase distortions in the spectra. These effects are the combined result of nonideal rf irradiation and hypercomplex data processing. The distortion effects have been analyzed in detail and general correction procedures that are both very efficient and accurate are suggested.

The general applicability of two-dimensional quadrupole-resolved one- and two-pulse ^{2}H MAS NMR spectroscopy has been demonstrated experimentally by acquiring a series of spectra of polycrystalline malonic-acid-$^2H_4$. It has been shown that the overlapping spinning sideband manifolds from the carboxyl and methylene deuterons can be separated completely. The spinning sideband manifolds have been analyzed to determine the quadrupole parameters for the carboxyl and methylene deuterons. The values agree with previous results and show that the techniques are both accurate and reliable. The spectra have been acquired with optimum pulse sequence parameters. It has been shown that the experimentally determined pulse sequence parameters agree with those calculated on the basis of the quadrupole parameters. It is noted that it is often difficult to determine the optimum pulse sequence parameters experimentally. This suggests that they should be calculated from the quadrupole parameters which can easily be determined from the spectra. In this approach the spectra are first acquired with a set of pulse sequence parameters that may not be optimum. From these spectra the quadrupole parameters

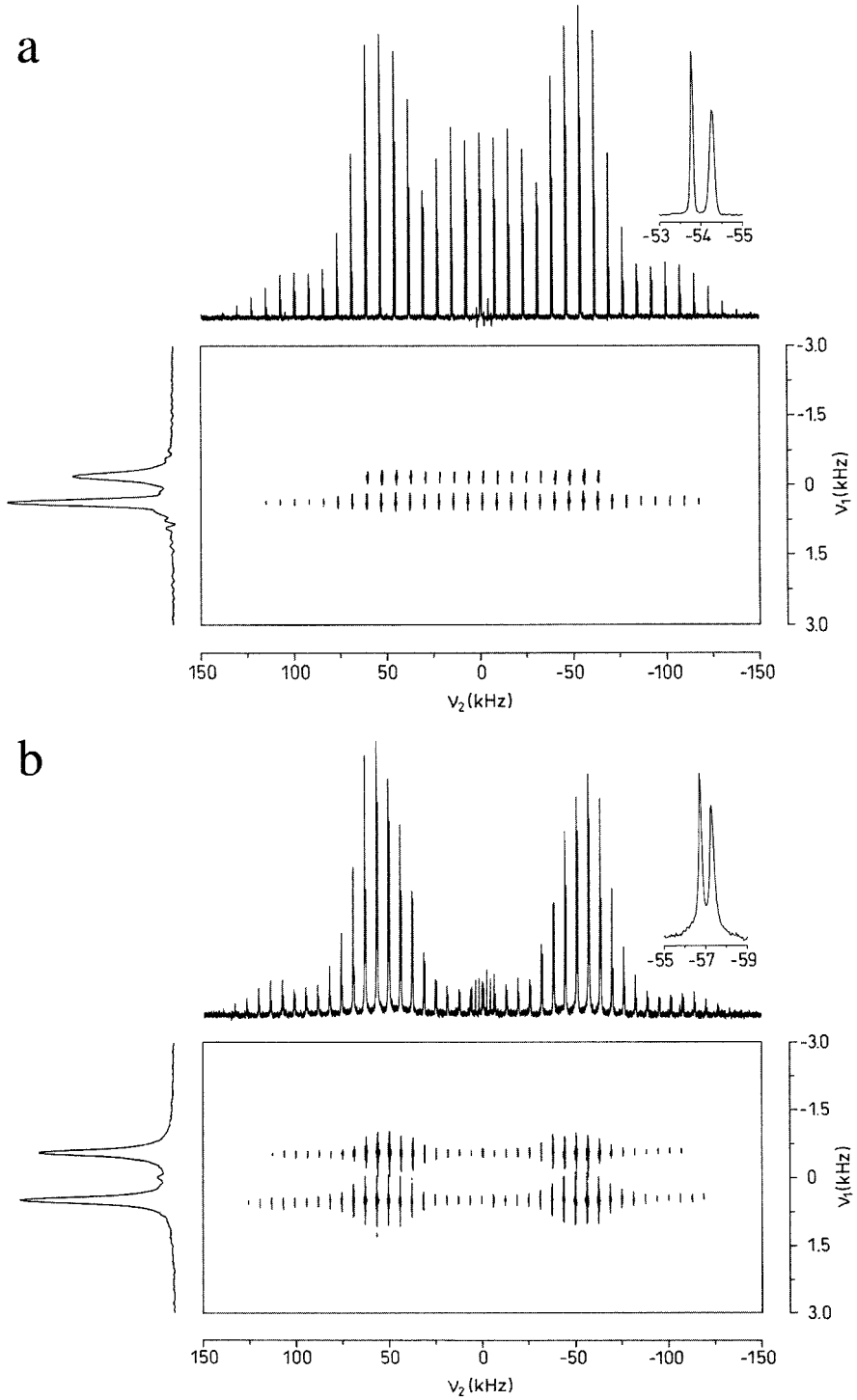

FIG. 9. Experimental (a) quadrupole-resolved two-pulse and (b) double-quantum ^{2}H MAS NMR spectra of polycrystalline malonic-acid-$^2H_4$. The experiments were performed on a Varian VXR 400 S spectrometer with rotation frequencies (a) $\nu_r = 7750$ Hz and (b) $\nu_r = 6350$ Hz. The rf field strengths were (a) $\nu_{rf} = 35.5 \pm 0.5$ kHz and (b) $\nu_{rf} = 31.5 \pm 0.5$ kHz. The optimum pulse sequence parameters were (a) $\tau^*_{p1} = 3.50 \pm 0.50$ μs and $\tau^*_{p2} = 3.50 \pm 0.50$ μs and (b) $\tau^*_{p1} = 5.25 \pm 0.50$ μs, $\tau^*_{p2} = 5.25 \pm 0.50$ μs, $\tau^*_{p3} = 5.00 \pm 0.50$ μs, and $\tau^*_{d} = 0.00 \pm 0.50$ μs. For quadrature detection in the evolution period two complementary experiments (Eq. [2]) were performed that differ by (a) $\frac{3\pi}{2}$ and (b) $\frac{3\pi}{4}$ in the phase of the preparation pulses.

are determined and an optimum set of pulse sequence parameters is calculated. The experiments are then repeated to obtain spectra with optimum resolution and sensitivity.

The performance of the quadrupole-resolved one- and two-pulse experiments has been shown to differ considerably. For both experiments the spinning sidebands are composed of

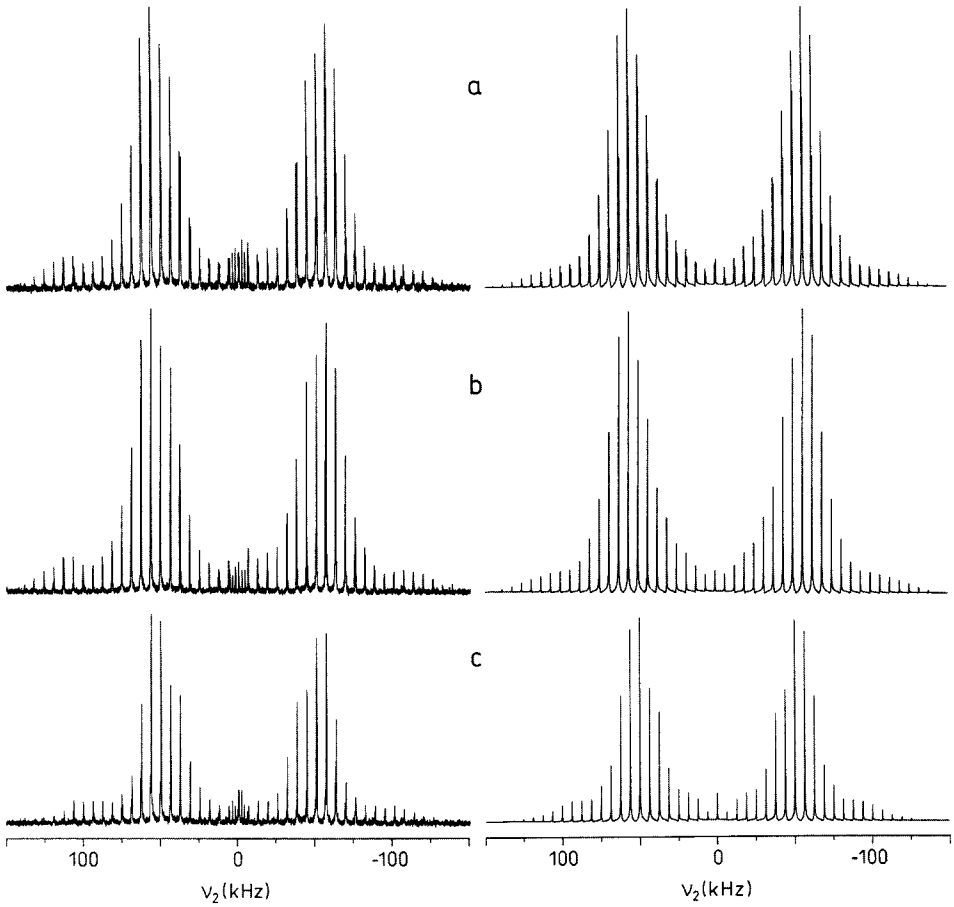

FIG. 10. Experimental (left column) and theoretical (right column) ω_2 projections for polycrystalline malonic-acid-$^2H_4$. The projections were obtained from the double-quantum ^{2}H MAS NMR experiment. The calculations employed the quadrupole coupling constant $C_Q = 181$ kHz and asymmetry parameter $\eta_Q = 0.11$ for the carboxyl deuterons while $C_Q = 166$ kHz and $\eta_Q = 0.00$ for the methylene deuterons.

absorption–absorption, absorption–dispersion, dispersion–absorption, and dispersion–dispersion lineshapes (*15–17*). For the one-pulse experiment the proportion of absorption components is identical to the proportion of dispersion components and independent of the rf field strength. This is different from the two-pulse experiment where the proportion of absorption components is much larger than the proportion of dispersion components. The resolving power is therefore highest for the two-pulse experiment. However, the sensitivity is much higher for the one-pulse experiment than is preferred for systems with low sensitivity and widely separated isotropic shielding frequencies. The two-pulse experiment is most advantageous for systems with high sensitivity and closely spaced isotropic shielding frequencies.

Although the two-dimensional quadrupole-resolved two-pulse experiment improves the resolution significantly it may not be sufficient to separate overlapping spinning sideband manifolds for systems where the residual linewidth of the spinning sidebands is comparable to the differences in isotropic shielding frequency. This is important for structurally or dynamically disordered systems where the spinning sidebands may be extensively broadened (*19*). In order to improve the resolution the technique of two-dimensional double-quantum ^{2}H MAS NMR has previously been suggested (*20–23*). In this paper a hypercomplex version of the technique is developed and the intensity and phase characteristics are evaluated. It is shown that the technique may improve the resolution by a factor of 2 for systems with small quadrupole interactions. However, for large quadrupole interactions the resolution enhancement is much smaller and depends on the actual lineshape. The combined effect of nonideal rf irradiation and hypercomplex data processing leads to spinning sidebands composed of absorption–absorption, absorption–dispersion, dispersion–absorption, and dispersion–dispersion lineshapes. It is shown that the proportion of dispersion components is subject to variation by the pulse sequence parameters. This has led to a general methodology for evaluating the optimum pulse sequence parameters. The approach is demonstrated experimentally for polycrystalline malonic-acid-$^2H_4$.

ACKNOWLEDGMENTS

This work was supported by grants from the Danish Natural Science Research Council (11-9424-1 and 11-9424-2) to J.H.K.

REFERENCES

1. C. A. Fyfe, "Solid State NMR for Chemists," C. F. C. Press, Guelph (1983).
2. J. H. Davis, K. R. Jeffrey, M. Bloom, M. I. Valic, and T. P. Higgs, *Chem. Phys. Lett.* **42,** 390 (1976).
3. M. Bloom, J. H. Davis, and M. I. Valic, *Can. J. Phys.* **58,** 1510 (1980).
4. H. W. Spiess and H. Sillescu, *J. Magn. Reson.* **42,** 381 (1981).
5. J. L. Ackerman, R. Eckman, and A. Pines, *Chem. Phys.* **42,** 423 (1979).
6. N. J. Clayden, *Chem. Phys. Lett.* **131,** 517 (1986).
7. J. H. Kristensen, H. Bildsøe, H. J. Jakobsen, and N. C. Nielsen, *J. Magn. Reson.* **92,** 443 (1991).
8. A. J. Kim and L. G. Butler, *J. Magn. Reson.* **99,** 292 (1992).
9. R. Poupko, Z. Olender, D. Reichert, and Z. Luz, *J. Magn. Reson.* **106,** 113 (1994).
10. S. E. Woehler, R. J. Wittebort, S. M. Oh, D. N. Hendrickson, D. Inniss, and C. E. Strouse, *J. Am. Chem. Soc.* **108,** 2938 (1986).
11. D. R. Torgeson, R. J. Schoenberger, and R. G. Barnes, *J. Magn. Reson.* **68,** 85 (1986).
12. T. A. Early, *J. Magn. Reson.* **74,** 337 (1987).
13. R. R. Ernst, G. Bodenhausen, and A. Wokaun, "Principles of Nuclear Magnetic Resonance in One and Two Dimensions," Clarendon Press, Oxford (1987).
14. B. Blümich, P. Blümler, and J. Jansen, *Solid State Nucl. Magn. Reson.* **1,** 111 (1992).
15. G. Bodenhausen, H. Kogler, and R. R. Ernst, *J. Magn. Reson.* **58,** 370 (1984).
16. J. Keeler and D. Neuhaus, *J. Magn. Reson.* **63,** 454 (1985).
17. D. J. States, R. A. Haberkorn, and D. J. Ruben, *J. Magn. Reson.* **48,** 286 (1982).
18. T. P. Spaniol, A. Kubo, and T. Terao, *J. Chem. Phys.* **106,** 5393 (1997).
19. J. H. Kristensen, H. Bildsøe, H. J. Jakobsen, and N. C. Nielsen, *J. Magn. Reson.* **100,** 437 (1992).
20. R. Eckman, L. Müller, and A. Pines, *Chem. Phys. Lett.* **74,** 376 (1980).
21. L. Müller, *J. Magn. Reson.* **42,** 324 (1981).
22. N. Chandrakumar, G. von Firks, and H. Günther, *Magn. Reson. Chem.* **32,** 433 (1994).
23. M. J. Duer and C. Stourton, *J. Magn. Reson.* **129,** 44 (1997).
24. R. R. Ernst and W. A. Anderson, *Rev. Sci. Instrum.* **37,** 93 (1966).
25. G. Bodenhausen, R. L. Vold, and R. R. Vold, *J. Magn. Reson.* **37,** 93 (1980).
26. M. A. Delsuc, *J. Magn. Reson.* **77,** 119 (1988).
27. U. Fano, *Rev. Mod. Phys.* **29,** 74 (1957).
28. J. H. Kristensen, H. Bildsøe, H. J. Jakobsen, and N. C. Nielsen, *Prog. NMR Spectrosc.* **34,** 1 (1999).
29. M. M. Maricq and J. S. Waugh, *J. Chem. Phys.* **70,** 3300 (1979).
30. A. Samoson, E. Kundla, and E. Lippmaa, *J. Magn. Reson.* **49,** 350 (1982).
31. M. Munowitz, *J. Magn. Reson.* **73,** 338 (1987).
32. J. A. Goedkoop and C. H. MacGillavry, *Acta Crystallogr.* **10,** 125 (1957).
33. S. F. Sagnowski, S. Aravamudhan, and U. Haeberlen, *J. Magn. Reson.* **28,** 271 (1977).
34. W. Derbyshire, T. C. Gorvin, and D. Warner, *Mol. Phys.* **17,** 401 (1969).
35. R. N. Bracewell, "The Fourier Transform and Its Applications," McGraw–Hill, New York (1986).